Petroleum Science 23 (2026) 5928–5959

Contents lists available at ScienceDirect

Petroleum Science

journal homepage: www.keaipublishing.com/en/journals/petroleum-science

Original Paper

Experimental and simulation of nanofluid-enhanced tubular heating process for waxy crude oil storage tank

Jian Zhao [a,b,c], Zhen-Dong Yang [a,b,c], Fan Li [a,b,c], Hang Dong [a,b,c,*], Zhi-Hua Wang [a,b,c]

[a] School of Petroleum Engineering, Northeast Petroleum University, Daqing, 163318, Heilongjiang, China
[b] Center for Experimental Petroleum Engineering and Geology Education, Northeast Petroleum University, Daqing, 163318, Heilongjiang, China
[c] National Simulation Education Center for Oil and Gas Engineering, Northeast Petroleum University, Daqing, 163318, Heilongjiang, China

ARTICLE INFO

Article history:
Received 22 September 2025
Received in revised form
7 December 2025
Accepted 7 May 2026
Available online 14 May 2026

Edited by Min Li

Keywords:
Numerical simulation
Tubular heating
Nanofluid
Gel-sol transition
Heat transfer enhancement

ABSTRACT

Traditional tubular heating systems using water as the heat transfer fluid suffer from high energy consumption and uneven heating. This study proposes an innovative approach: employing nanofluids as a novel heat transfer fluid and developing a comprehensive numerical model capable of accurately describing the complex gel-sol transition behavior of waxy crude oil. The model characterizes the temperature-dependent viscosity of waxy crude oil using a hybrid Arrhenius + power law + Herschel-Bulkley model, accounts for phase change latent heat through the apparent heat capacity method, and calculates the thermal conductivity of waxy crude oil in different states using a weighted average method. Focusing on a floating roof tank equipped with a tubular heating system, nanofluids were prepared in-house and an indoor experimental system was constructed. The study investigated the temperature field, flow field, and gel-sol transition behavior of waxy crude oil during the tubular heating process within a small-scale model. Results indicated a relative deviation between experimental and simulation data within 4.61%. The findings demonstrated that CuO-water nanofluid significantly enhanced heating efficiency: it increased the heating rate of crude oil at the model bottom by 32% and at the top by 25%, reduced the thermal lag time by 15%, decreased the radial temperature difference by 1.2 °C, and accelerated the transition of crude oil from gel state through an intermediate state to sol state. Experiments also show that nanofluids exhibit significant heat transfer enhancement for crude oils with different properties, demonstrating good universality. Subsequently, the validated model and algorithm were employed to simulate the heating process in an actual size storage tank using different nanofluids. The simulations revealed the synergistic heat transfer enhancement mechanism of the nanofluid. Benefiting from superior thermal conductivity and a moderate specific heat capacity, it retards its own temperature drop and thins the thermal boundary layer inside the tube (CuO-water nanofluid reduced the thickness by 25%), and enhanced natural convection outside the tubes, achieving synergistic heat transfer enhancement on both sides. CuO-water nanofluid exhibited the best heat transfer enhancement performance. Although it did not alter the macroscopic structure of the temperature field, it increased the average heating rate of the crude oil by 16%, improved heating efficiency by 3.88%, and is projected to reduce heating energy consumption by 3.1% and carbon emissions by 4.9%. Simulations further reveal that optimized heating tube layout combined with nanofluids yields a synergistic enhancement effect, further elevating the overall tank temperature and reducing the low-temperature zone. This study provides not only a validated optimization methodology but also delivers fundamental insights and a theoretical framework for the technological innovation of tank heating systems. Furthermore, it extends the application of nanofluid-enhanced heat transfer technology to media including crude oil, which exhibits a range of rheological properties from Newtonian to non-Newtonian behavior, thereby broadening its scope of engineering applications.

* Corresponding author.
E-mail address: dh.123@163.com (H. Dong).
Peer review under the responsibility of China University of Petroleum (Beijing).

https://doi.org/10.1016/j.petsci.2026.05.006
1995-8226/

Nomenclature:

A_{mush}	Fuzzy zone constant
c_p	Specific heat of crude oil, J/(Kg·K)
H	Total enthalpy
H_{tank}	Tank height, m
R_{heat}	Inner diameter of heating tube, m
T	Temperature, °C
h	Convective heat transfer coefficient, W/(m^2·K)
ρ	Density, kg/m^3
u	Velocity, m/s
β	Thermal expansivity, 1/°C
γ	Shearing rate, s^{-1}
δ_{th}	Thermal boundary layer
δ_v	Velocity boundary layer
λ	Thermal conductivity, W/(m·K)
R_{tank}	Radius of storage tank, m
μ	Dynamic viscosity of fluid, Pa·s

Subscripts

l	Liquid phase
basewall	Base wall of the tank/beaker
heat	Heating tube
nf	Nanofluid
o	Crude oil
s	Solid phase
sidewall	Sidewall of the tank/beaker
topwall	Top wall of the tank/beaker
tank	Oil storage tank
w	Water

1. Introduction

Petroleum is an important energy pillar for global economic development. According to BP (2023), the demand for oil will continue to rise in the next decade. At the same time, the safe storage of oil is of vital importance to a country's energy security and economic lifeline (Ge, 2024). The crude oil in China is mostly of high wax content type, with a relatively high gel point. During the storage and transportation process, when the oil temperature is lower than the wax crystallization point, wax crystals precipitate and form a three-dimensional network structure, resulting in a significant increase in viscosity and deterioration of fluidity, which is prone to cause tank freezing accidents (Dong et al., 2025). In engineering, tubular heating technology is often adopted to assist in heating crude oil in tanks to prevent accidents. This technology, characterized by its compact structure, high thermal efficiency, and reliable operation, is widely used for anti-freezing and insulation protection of various storage tanks.

In recent years, through numerical simulations and field tests, scholars have investigated the gelation behavior of waxy crude oil (with a high gel point of 34 °C) in floating roof tanks (1000 and 10,000 m^3) in high-altitude and cold regions (with ambient temperatures as low as −20 °C), as well as the heat transfer and flow characteristics under different tubular heating methods. They have established relevant physical and mathematical models, analyzed the evolution of temperature distribution and flow pattern relationships, and explored the role of mechanical agitation coupled with heating, with 350 rpm identified as the optimal speed (Zhao, 2013; Zhao et al., 2017a; 2017b, 2020; 2023a; 2023b; 2025a; 2025b). Other scholars have also incorporated factors such as steam pressure (0.3–0.9 MPa), ambient temperature (10–30 °C), and solar radiation into their theoretical models for tubular heating in floating roof tanks, thereby revealing the evolution of the temperature field under these influences (Sun et al., 2016, 2021, 2023; Xie et al., 2021). Regarding the coupling between forced convection inside the heating tubes and natural convection outside, Zhao (2021) investigated the heat transfer characteristics of tubular heating under different parameters. This was done by combining PIV and thermocouple techniques with three-dimensional simulations and experiments, providing a systematic analysis. In the realm of parameter and structural optimization, scholarly investigations have encompassed diverse aspects. These include a hybrid heating method combining jet and tubular heating with mechanical stirring in a 1000 m^3 floating roof tank, for which an economic performance metric was proposed (Lei et al., 2024); the influence of heating tube diameter (76, 108, 159, 219 mm), layout position, and structural optimization of heating tube on the crude oil temperature field (Wang, 2018; Dong et al., 2023); the efficacy of coiled-tube structures with varying numbers of external fins (Wu, 2022); the analysis of tubular heating processes utilizing thermal oil at 380 °C (Ma et al., 2020); and the development of corresponding calculation methods for both steam and thermal oil as heating media (Yu, 2014).

In summary, the existing body of work primarily investigates these following categories of parameters: (i) structural parameters, such as the diameter and layout of the heating tubes, and presence of fins; (ii) operational parameters, including the type of heat transfer fluid (e.g., steam or thermal oil), its inlet temperature and flow rate, as well as external conditions like ambient temperature, wind speed, and solar radiation; and (iii) crude oil properties, notably the gel point and specific heat capacity. These factors collectively govern the temperature and flow field distributions inside the tank, which ultimately determine the heating efficiency and operational safety.

The actual waxy crude oil is a complex fluid that encompasses both Newtonian and non-Newtonian fluid characteristics. However, prevailing studies exhibit notable limitations: (i) most models oversimplify the heating tube walls as constant-temperature boundaries, failing to adequately capture the dynamic impact of the thermal medium's temperature drop along the tube on the external temperature field, (ii) the coupled effects of the gel-sol transition, non-Newtonian rheological behavior, and phase-change latent heat of waxy crude oil near its pour point are insufficiently characterized. These are also the starting points of this study.

To address these constraints of conventional tubular heating, scholars have explored various enhanced heat transfer strategies. For instance, electromagnetic heating technology, valued for its non-contact nature, high efficiency, and strong controllability, has demonstrated potential in pipeline and oil well applications for viscosity reduction and wax deposition mitigation in heavy oil (Zhao, 2024; Gao et al., 2024, 2025). However, retrofitting large-scale storage tanks for electromagnetic heating often entails prohibitively high costs and significant engineering complexities. In this context, employing high-performance heat transfer fluids to enhance efficiency at the source presents a more practical and promising pathway. As a novel enhanced heat transfer fluid, nanofluid—which work by dispersing nanoparticles to improve the base fluid's thermal conductivity and convective heat transfer coefficient, offer a significant performance boost (Ma et al., 2023).

Scholars has extensively quantified the behavior of nanofluid under key parameters, including magnetic field inclination ($\gamma = 0°–90°$), Rayleigh number ($Ra = 10^3–10^6$), and nanoparticle volume fraction ($\phi = 0–0.06$), to understand their natural convection characteristics (Sun et al., 2015; Hu et al., 2024; Saleem et al., 2023). Subsequent investigations have delved into their fundamental flow and heat transfer mechanisms within straight tubes (Yang et al., 2020), as well as their enhanced performance in more complex geometries like spring tubes compared to deionized water (Li et al., 2020). For more significant thermal enhancement, composite methods have been explored, such as hybrid nanofluids (Li, 2023; Fang, 2025), synergizing nanofluids with chaotic advection (e.g., in L-shaped chaotic flow channels) and magnetic fields (encompassing both constant non-uniform and alternating fields) (Wei, 2022). Furthermore, the heat transfer and flow resistance performance of various nanofluids have been systematically evaluated from multiple perspectives (Sahin et al., 2015; Naik et al., 2020; Patil and Shankar, 2022). Despite the significant potential of novel heat-transfer media like nanofluids in enhanced heat transfer, their application in the tubular heating of oil storage tanks remains scarcely explored. Research that integrates them with the complex phase-change processes of waxy crude oil is particularly lacking.

Based on the foregoing, this study aims to systematically evaluate the efficacy and mechanisms of nanofluids in the tubular heating process of waxy crude oil storage tanks. The objective of this study is threefold: (i) fully considering the gel-sol transition of waxy crude oil, non-Newtonian rheological properties and latent heat of phase change, and using the method combining experiments and numerical simulations to describe the flow, heat transfer and transition laws of waxy crude oil near the gel point, (ii) during the gel-sol transition of waxy crude oil, focusing on analyzing the influence of different nanofluids as heat transfer fluid on the conversion of crude oil, natural convection and the evolution of temperature uniformity, (iii) for actual size oil storage tank, using numerical simulation to comprehensively evaluate the heating effect of different nanofluids as heat transfer fluid and analyze the mechanism of enhanced heat transfer. Through the above research, it is expected to provide theoretical basis and reference for the optimization and innovation of heating technology for crude oil storage tank.

2. Experiments and numerical simulations of small-scale models

The heating process of crude oil in storage tank is essentially a natural convection effect triggered by a heat source. However, considering the large scale of actual storage tank and the high difficulty of experiments, the analysis was first conducted through experiments on small-scale models, and a corresponding numerical model was established.

2.1. Experimental setup and methods

The CuO-water nanofluid and graphene-water nanofluid with a concentration of 0.1% mol were prepared by using a two-step method. The instruments and supplies used are shown in Fig. 1, and the heat transfer fluid used in the experiment is shown in Fig. 2.

The morphology of CuO and graphene nanoparticles was observed using a “HITACHI-SU8010” scanning electron microscope (Fig. 1(e)), and the obtained SEM images are shown in Fig. 3. CuO nanoparticles are approximately spherical in shape, with primary particle sizes mainly distributed in the range of 40–50 nm. The graphene nanosheets used exhibit a typical wrinkled sheet-like

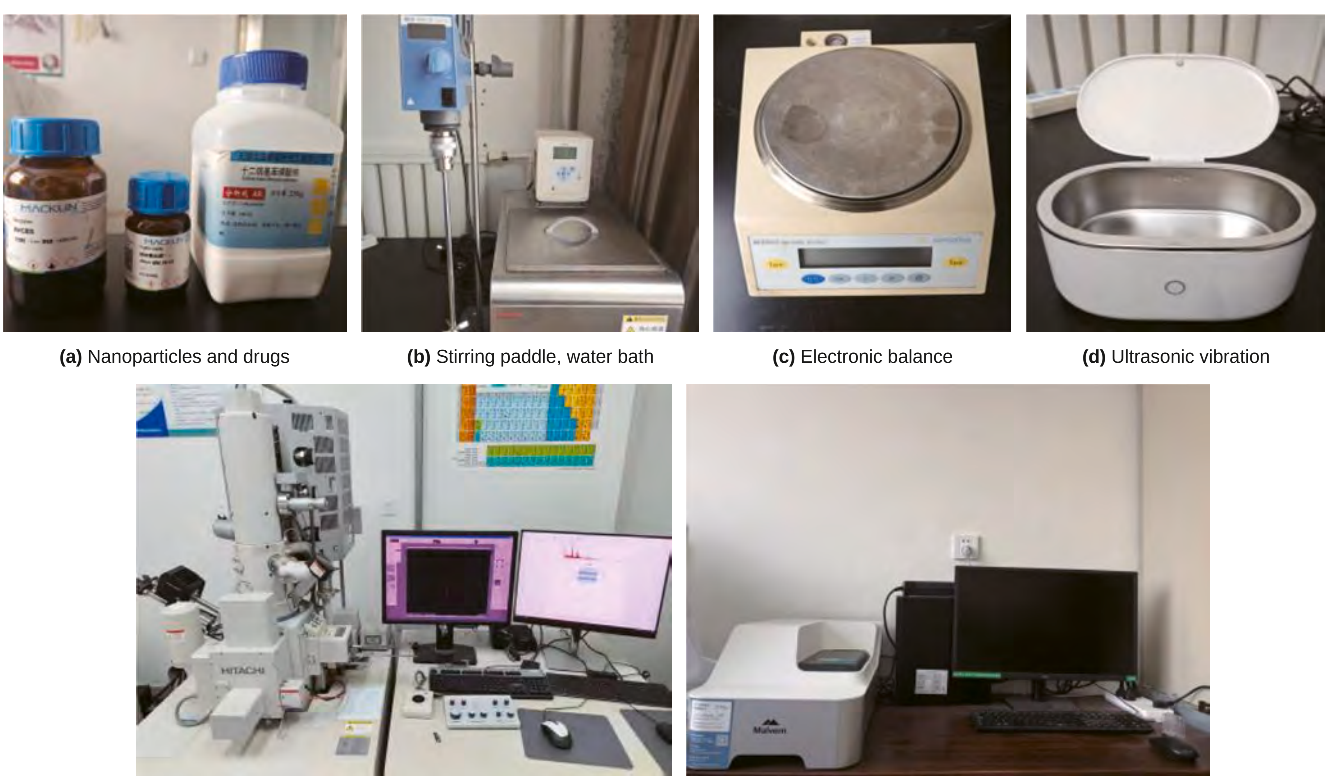

(a) Nanoparticles and drugs　**(b)** Stirring paddle, water bath　**(c)** Electronic balance　**(d)** Ultrasonic vibration

(e) Scanning electron microscope　**(f)** Dynamic light scattering instrument

Fig. 1. Equipment required for configuring nanofluids.

(a) Water **(b)** Graphene-water nanofluid **(c)** CuO-water nanofluid

Fig. 2. Heat transfer fluid used in the experiment.

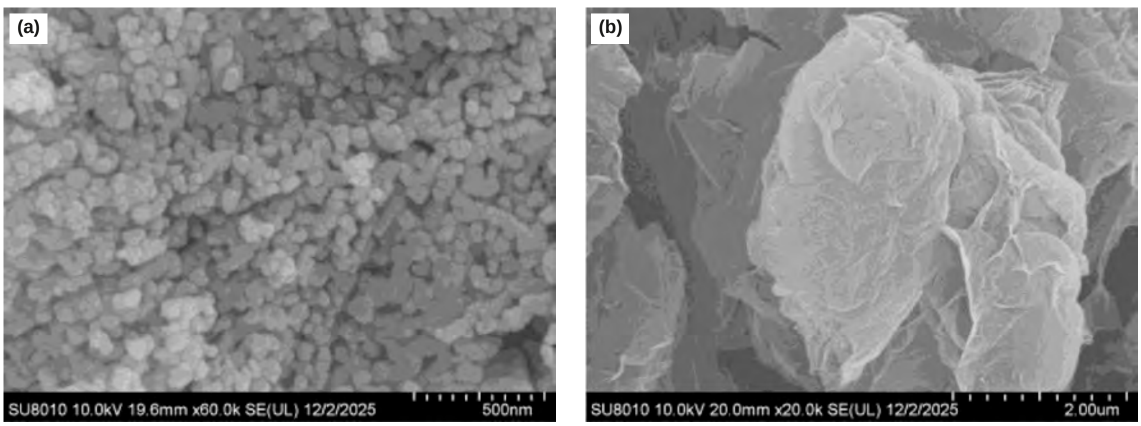

Fig. 3. SEM images of nanoparticles. **(a)** CuO, **(b)** graphene.

structure, lateral dimensions ranging from several hundred nanometers to the micrometer scale.

To quantitatively evaluate the suspension stability of nanofluid, this study employed a static sedimentation height-based evaluation method (Fang, 2025). The sedimentation rate K is calculated as follows:

$$K = L/L_0 \tag{1}$$

where K is the sedimentation rate (a smaller value indicates better stability), L_0 is the height of the clear supernatant after settling (mm), and L is the total initial height of the nanofluid suspension (mm). It is generally accepted that $K \leq 0.3$ indicates extremely high stability, while $K \geq 0.65$ suggests that stability is essentially lost. The sedimentation rate curves of the two nanofluids over time are shown in Fig. 4. After 3 days of static settling, the K values for both CuO-water nanofluid and graphene-water nanofluid approach 0.65, indicating significant sedimentation and a decline in stability over this timeframe. Notably, the graphene-water nanofluid exhibits a higher sedimentation rate.

Furthermore, the dispersion state of the nanoparticles in the fluid was further analyzed using a "Malvern Zetasizer Lab" (Fig. 1(f)) dynamic light scattering instrument (Fig. 5). The DLS results show that the graphene-water nanofluid has a particle size of 197.6 nm, with a secondary peak present at 893.8 nm. This indicates the formation of aggregates due to face-to-face stacking of graphene nanosheets. In contrast, the CuO-water nanofluid shows a particle size of 50.79 nm, consistent with the primary particle size observed via SEM. To simulate the long-term shear and thermal effects under actual operating conditions, an isothermal circulation test was conducted on CuO-water nanofluid for 36 h. The post-circulation DLS curve (Fig. 5) reveals only a slight rightward shift in the particle size distribution. The particle size increased to 68.69 nm, with no drastic or abrupt changes observed in the size distribution profile. This suggests that while unavoidable aggregation occurs in the CuO-water nanofluid under prolonged circulation, it maintains relatively good dynamic stability, likely due to the thermal-shear effects present during the circulation process.

The two prepared nanofluids and water were heated to 70 °C in a constant temperature water bath. The inlet and outlet of the heating tube were connected by a micro peristaltic pump. The heating tube was placed at the bottom of the device to transport the heat transfer fluid. 3 L of crude oil (liquid level is 13.5 cm) was poured in, which had been heated to a uniform temperature beforehand. A JTR type temperature recorder was used to collect temperature data at 30-s intervals. Multiple sensor measurement points were arranged in the experimental device (as shown in Fig. 6). To reduce the influence of the inherent accuracy of the instrument and measurement errors, the density of the measurement points was increased, and they were respectively located at heights of 2.5, 5, 7.5, and 10 cm from the bottom.

The experimental process and equipment are shown in Figs. 7 and 8. The measuring instruments were calibrated in accordance with JJF 1366-2012 "Calibration Specification for Temperature Data Acquisition Instruments". The results showed that the measured values of the thermometer and the sensor were highly consistent, with the error being less than 0.1%. During the experiment, the environmental temperature was maintained at (25 ± 0.5) °C, and the initial temperature of the crude oil reached 25 °C after standing still. After heating the three heat transfer fluid to 70 °C, they were introduced into the heating tube to heat the crude

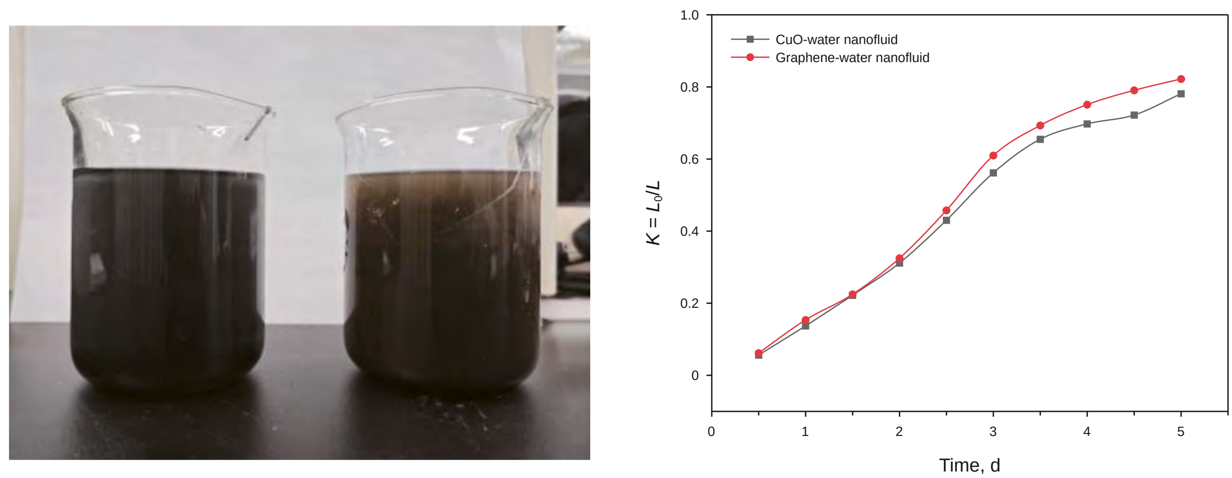

(a) Nanofluids (b) Settling rate

Fig. 4. Settling rate of nanofluids. **(a)** Nanofluids, **(b)** settling rate.

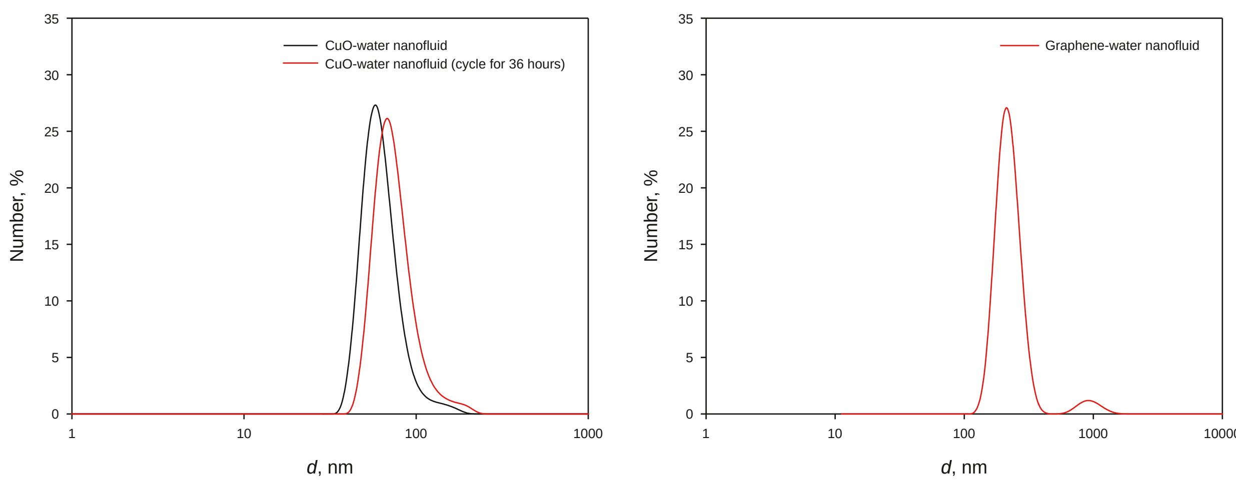

(a) CuO-water nanofluid **(b)** Graphene-water nanofluid

Fig. 5. Particle size distribution of nanofluids.

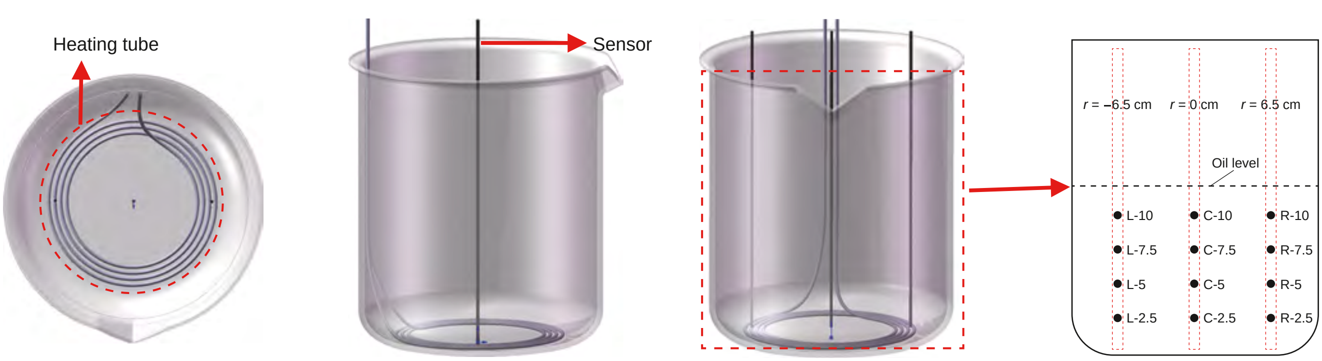

(a) Top view **(b)** Side view **(c)** Front view **(d)** Sensor position

Fig. 6. Experimental device model and distribution of temperature measurement points.

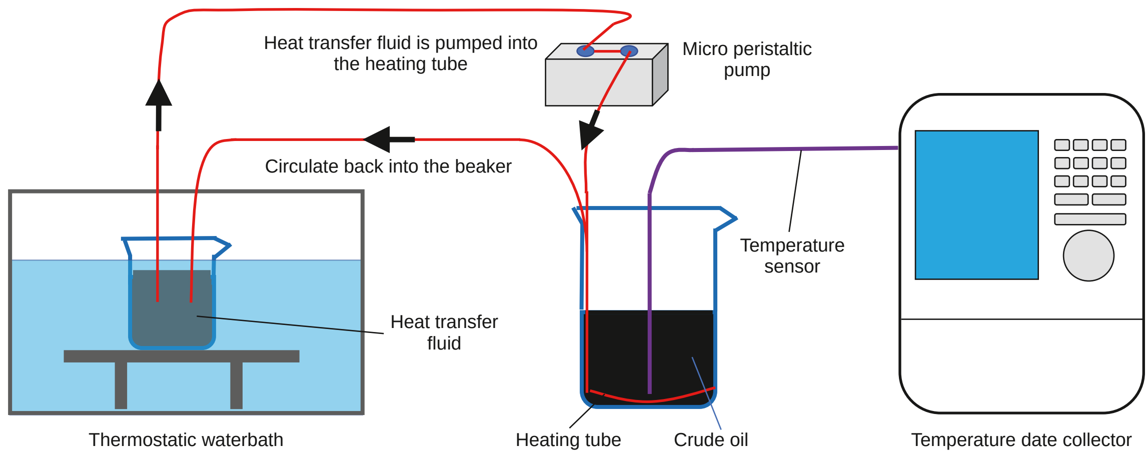

Fig. 7. Heating experiment flowchart.

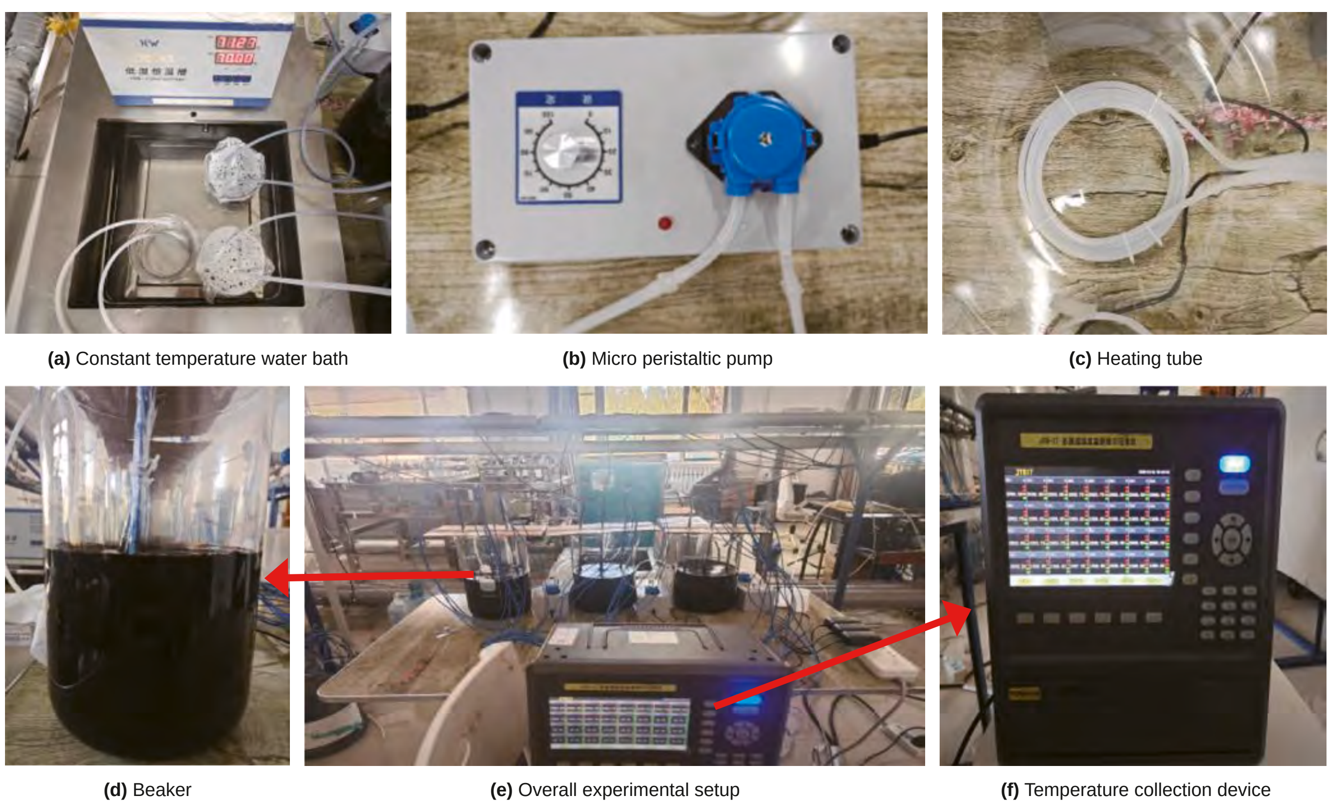

Fig. 8. Experimental setup.

oil. Due to the different thermophysical properties of the heat transfer fluid, different heating times were set to make the overall temperature consistent.

2.2. Numerical simulation method

2.2.1. Governing equations

For the numerical simulation of three-dimensional tubular heating, the corresponding governing equations need to be provided.

(1) Equation of continuity:

$$\frac{\partial \rho}{\partial t}+\nabla\cdot\boldsymbol{v}=0 \tag{2}$$

(2) Momentum equation:

$$\rho\left(\frac{\partial \boldsymbol{v}}{\partial t}+\boldsymbol{v}\cdot\nabla\boldsymbol{v}\right)=-\nabla p+\nabla\cdot\boldsymbol{\tau}+\rho g+\mathbf{S} \tag{3}$$

Source term of the momentum equation:

$$\mathbf{S}_v=-\frac{(1-\beta)^2}{\left(\beta^3+\varepsilon\right)}A_{\text{mush}}\boldsymbol{v} \tag{4}$$

β represents the liquid phase fraction:

$$\beta = \begin{cases} 0 & T < T_\mathrm{s} \\ T - T_\mathrm{s}/T_\mathrm{l} - T_\mathrm{s} & T_\mathrm{s} \le T \le T_\mathrm{l} \\ 1 & T > T_\mathrm{l} \end{cases} \tag{5}$$

when $\beta = 0$, it is pure solid; when $\beta = 1$, it is pure liquid. At this point, the momentum equation reverts to the standard form; when $0 < \beta < 1$, it is paste-like region. The relationship between the stress tensor and the strain rate tensor D:

$$\boldsymbol{\tau} = 2\mu \boldsymbol{D} \tag{6}$$

$$\boldsymbol{D} = \frac{\nabla \boldsymbol{u} + (\nabla \boldsymbol{u})^T}{2} \tag{7}$$

(3) Energy equation:

$$\frac{\partial(\rho H)}{\partial t} + \nabla \cdot (\rho \boldsymbol{v} H) = \nabla \cdot \left(\frac{k}{c_{\boldsymbol{p}}} \cdot \nabla H \right) \tag{8}$$

2.2.2. Nanofluid flow and heat transfer model

This study treats nanofluids using a homogeneous single-phase fluid model. It is important to note that the effective property correlations employed are based on the assumption of a static, homogeneous suspension, which introduces certain limitations. This approach cannot capture micro-scale phenomena such as nanoparticle migration and aggregation that may occur during flow. These phenomena can lead to spatial inhomogeneity in local particle concentration, while nanoparticle aggregation may enhance the thermal conductivity of the nanofluid (Wang et al., 2022; Chen et al., 2023). However, as the primary objective of this study is to compare the heating performance of different nanofluids rather than to precisely predict micro-scale particle dynamics, coupled with the low nanoparticle concentrations utilized, the single-phase model is considered appropriate and effective in this context. The flow and heat transfer of nanofluids still obey the conservation laws of mass, momentum, and energy. The continuity equation:

$$\frac{\partial \rho_\mathrm{nf}}{\partial t} + \nabla \cdot \left(\rho_\mathrm{nf} \boldsymbol{v}_\mathrm{nf} \right) = 0 \tag{9}$$

Momentum equation:

$$\frac{\partial \left(\rho_\mathrm{nf} \boldsymbol{v}_\mathrm{nf} \right)}{\partial t} + \nabla \left(\rho_\mathrm{nf} \boldsymbol{v}_\mathrm{nf} \boldsymbol{v}_\mathrm{nf} \right) = -\nabla p + \nabla \cdot \left(\mu_\mathrm{nf} \nabla \boldsymbol{v}_\mathrm{nf} \right) + \rho g \tag{10}$$

Energy equation:

$$\frac{\partial \left(\rho_\mathrm{nf} c_\mathrm{p,nf} T \right)}{\partial t} + \nabla \left(\rho_\mathrm{nf} c_\mathrm{p,nf} \boldsymbol{v}_\mathrm{nf} T \right) = \nabla \left(k_\mathrm{nf} \nabla T \right) \tag{11}$$

2.2.3. Boundary conditions

(1) The sidewall and basewall of the beaker, with a thickness of 0.003 m, as well as the oil surface and air layer with a thickness of 0.135 m, are all defined as third boundary condition. The ambient temperature is 25 °C and convective heat transfer coefficients are specified as 13.5, 0.5, and 15 W/($\mathrm{m}^2 \cdot \mathrm{K}$) for these boundaries, respectively.

$$h = H_\mathrm{beaker}, 0 \le r \le R_\mathrm{beaker}, -\lambda_\mathrm{topwall} \frac{\partial T_\mathrm{topwall}}{\partial h} = h_\mathrm{topwall} \left(T_\mathrm{topwall} - T_\mathrm{air} \right), u_\mathrm{topwall} = 0 \tag{12}$$

$$0 \le h \le H_\mathrm{beaker}, r = R_\mathrm{beaker}, -\lambda_\mathrm{sidewall} \frac{\partial T_\mathrm{sidewall}}{\partial h} = h_\mathrm{sidewall} (T_\mathrm{sidewall} - T_\mathrm{air}), u_\mathrm{sidewall} = 0 \tag{13}$$

$$h = 0, 0 \le r \le R_\mathrm{beaker}, -\lambda_\mathrm{basewall} \frac{\partial T_\mathrm{basewall}}{\partial h} = h_\mathrm{basewall} (T_\mathrm{basewall} - T_\mathrm{air}), u_\mathrm{basewall} = 0 \tag{14}$$

(2) a_heat and b_heat are the coordinates of the center of the cross-section of the heating tube. The inlet cross-section of the heating tube is defined as velocity inlet boundary, u_in = 0.236 m/s, T_heat = 70 °C:

$$(r - a_\mathrm{heat})^2 + (h - b_\mathrm{heat})^2 = R_\mathrm{heat}^2, T_\mathrm{water} = T_\mathrm{heat}, u_\mathrm{in} = u_\mathrm{heat} \tag{15}$$

(3) The exit cross-section of the heating tube is defined as outflow boundary:

$$(r - a_\mathrm{heat})^2 + (h - b_\mathrm{heat})^2 = R_\mathrm{heat}^2, \frac{\partial u_\mathrm{out}}{\partial n} = 0 \tag{16}$$

(4) The contact boundary at the inner wall of the heating tube is defined as a fluid-solid conjugate heat transfer interface:

$$(r - a_\mathrm{heat})^2 + (h - b_\mathrm{heat})^2 = R_\mathrm{heat}^2, -\lambda_\mathrm{heatwall} \frac{\partial T_\mathrm{heatwall}}{\partial r} = h_\mathrm{water} (T_\mathrm{heatwall} - T_\mathrm{water}) \tag{17}$$

$$(r - a_\mathrm{heat})^2 + (h - b_\mathrm{heat})^2 = R_\mathrm{heat}^2, -\lambda_\mathrm{heatwall} \frac{\partial T_\mathrm{heatwall}}{\partial h} = h_\mathrm{water} (T_\mathrm{heatwall} - T_\mathrm{water}) \tag{18}$$

(5) The contact boundary at the outer wall of the heating tube is defined as a fluid-solid conjugate heat transfer interface, Φ = 0.003 m:

$$(r - a_\mathrm{heat})^2 + (h - b_\mathrm{heat})^2 = (R_\mathrm{heat} + \Phi)^2, -\lambda_\mathrm{heatwall} \frac{\partial T_\mathrm{heatwall}}{\partial r} = h_\mathrm{oil} (T_\mathrm{heatwall} - T) \tag{19}$$

$$(r - a_\mathrm{heat})^2 + (h - b_\mathrm{heat})^2 = (R_\mathrm{heat} + \Phi)^2, -\lambda_\mathrm{heatwall} \frac{\partial T_\mathrm{heatwall}}{\partial h} = h_\mathrm{oil} (T_\mathrm{heatwall} - T) \tag{20}$$

2.2.4. Numerical model

Based on the geometric structure and boundary conditions of the aforementioned experimental setup, areas such as the bent part of the beaker's rim were simplified. A corresponding three-dimensional numerical model and grid system were established (Fig. 9), and temperature collection points corresponding to the experimental monitoring points were set in the numerical simulation.

2.3. Properties of waxy crude oil and heat transfer fluid

Using waxy crude oil as the simulation medium, its rheological and thermophysical properties change complexly with temperature. When the temperature is higher than the wax precipitation point, the wax is completely dissolved, and the crude oil forms a single-phase system (as shown in the in-situ microscopic observation results in reference (Dong et al., 2025)), behaving as a Newtonian fluid, with viscosity affected by temperature. When the temperature drops to the wax precipitation point, the wax begins to crystallize and precipitate, accompanied by latent heat release, and the viscosity of the system increases. As the temperature drops to the abnormal point, the system changes from a Newtonian fluid to a non-Newtonian fluid. The viscosity is influenced by both temperature and shear rate. When the temperature drops further and approaches the loss-of-flow point, the flocculation between wax crystals forms a three-dimensional network structure. The wax crystals act as the framework, while the liquid oil is embedded in the pores. The system transforms into a gel system resembling a porous medium. In order to maintain consistency with the experimental conditions, in the simulation, the initial temperature of the crude oil was set at 25 °C, at which point the crude oil was in a gel state. As the heating process continues, the crude oil gradually transforms from gel to sol state, and its rheological properties and thermal physical properties undergo significant changes. This study first measured the temperature-dependent viscosity behavior of waxy crude oil using a QC rotational rheometer. Subsequently, differential scanning calorimetry (DSC) tests were conducted in accordance with the SY/T 0545-2012 standard to determine the wax precipitation point and calculate the wax content. The specific considerations are as follows:

(1) In previous studies, the thermal conductivity of waxy crude oil was mostly assumed to be a constant value., resulting in a certain gap between the simulated temperature values and the actual measured values. Therefore, the influence of wax

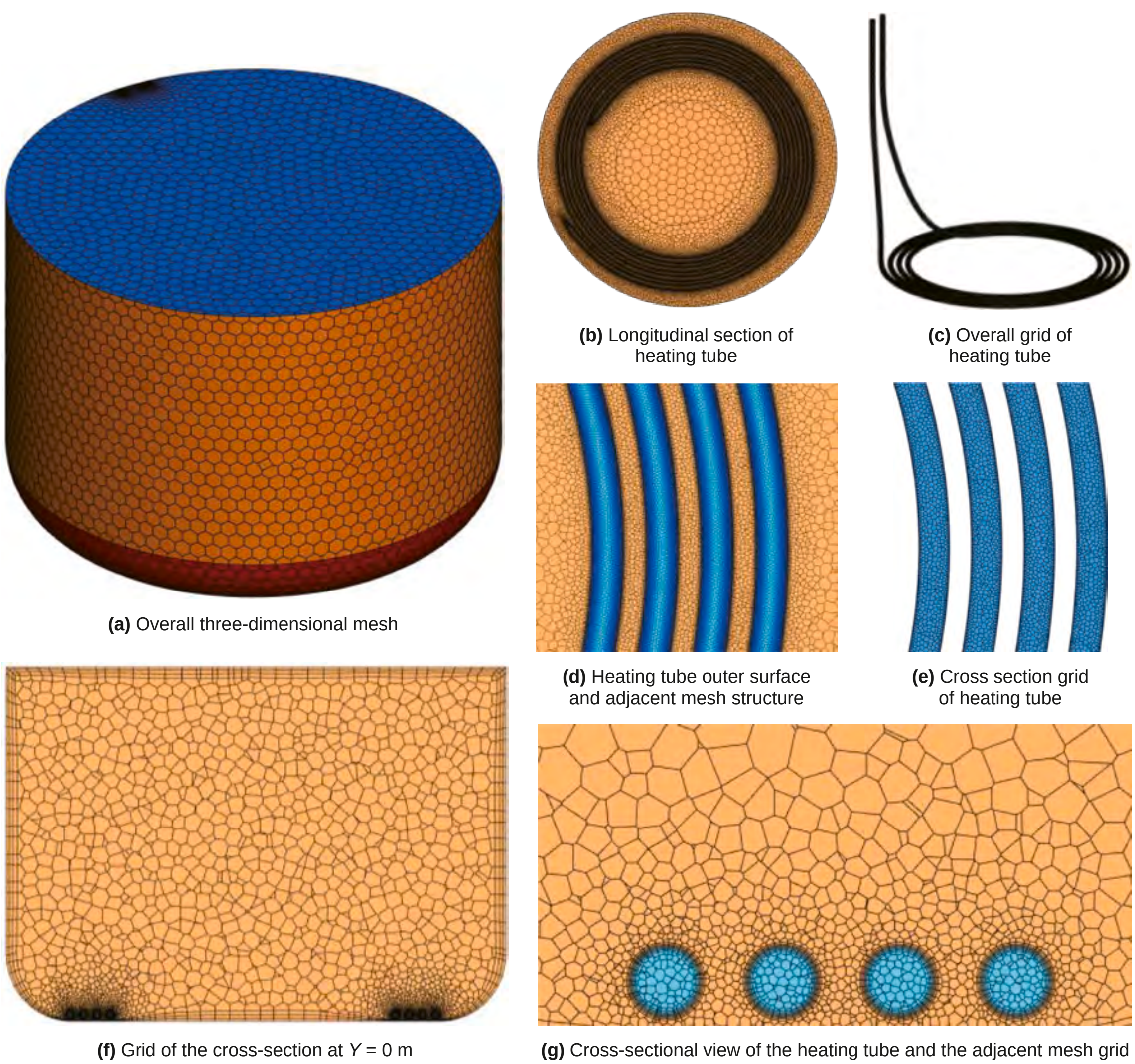

Fig. 9. Numerical calculation domain and its grid system.

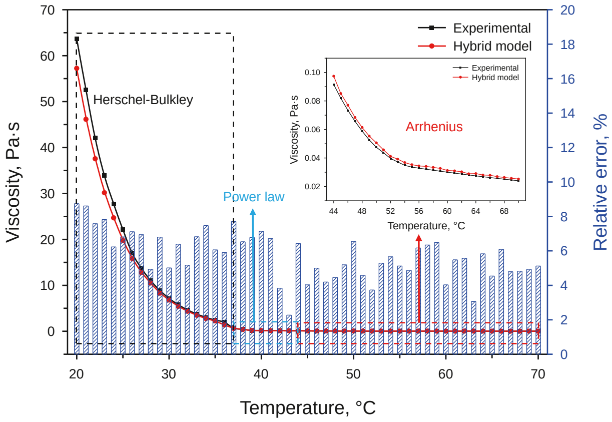

Fig. 10. Experimentally measured viscosity and hybrid model-predicted viscosity.

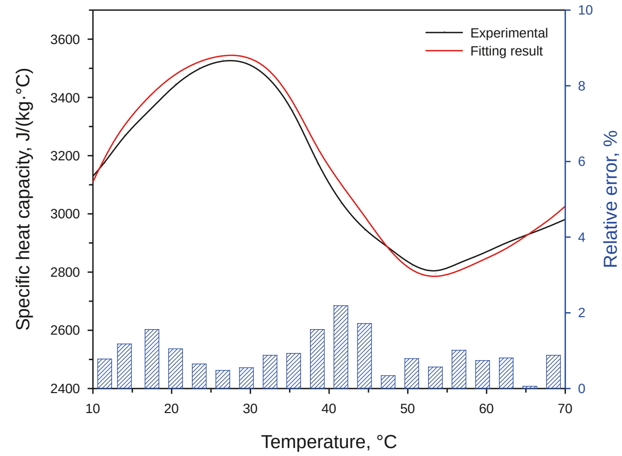

Fig. 11. Specific heat capacity of waxy crude oil.

precipitation needs to be taken into account in the variation of the thermal conductivity of crude oil. Based on the corresponding relationship between the wax precipitation amount of crude oil and temperature, with a liquid oil thermal conductivity of 0.14 W/(m·K) (Dong et al., 2025), a wax content of 2.5% in the gelled crude oil, and assuming a paraffin thermal conductivity of 2.5 W/(m·K), the weighted calculation using Eq. (21) yields the thermal conductivity of gelled crude oil as 0.2 W/(m·K), and its thermal conductivity in the sol state as 0.14 W/(m·K).

$$\lambda = \left(1 - \alpha_{\text{paraffin}}\right)\lambda_{\text{oil}} + \alpha_{\text{paraffin}}\lambda_{\text{paraffin}} \tag{21}$$

(2) Relying on the experimentally obtained rheological data, the viscosity of the waxy crude oil is calculated according to Eq. (22). When the temperature is higher than 55 °C (the wax precipitation point), the waxy crude oil is Newtonian fluid and its viscosity is calculated using the Arrhenius model. When the temperature is between the wax precipitation point and the anomalous point (44 °C), the viscosity is still calculated using the Arrhenius model, but the exponent changes. When the temperature is lower than the anomalous point, the viscosity is characterized by the power law model. When the temperature is between the loss flow point (37 °C) and 20 °C, the viscosity is characterized by the Herschel-Bulkley model, Fig. 10 shows a comparison between the experimentally measured viscosity and the viscosity predicted by the hybrid model. The data cover a temperature range from 20 to 70 °C at a shear rate of 10 s^{-1}. Different colored dashed boxes indicate data from different temperature intervals: black (20–37 °C, Herschel-Bulkley model), blue (37–44 °C, power law model), and red (>44 °C, Arrhenius model). The calculated mean relative deviation for all data points is 7.2%, demonstrating that the hybrid model reliably describes the rheological behavior of the waxy crude oil. At the same time, using the porous medium method, the additional resistance of the wax crystal network structure within the gelled crude oil to the system flow was characterized by adding additional source terms to the momentum equation (Eqs. (3) and (4)), thereby making the simulation results closer to the actual situation.

(3) Based on the experimentally measured DSC data, Eq. (23) was fitted to describe the temperature dependence of the specific heat capacity of waxy crude oil, the latent heat of the wax crystals is characterized in the variation of specific heat capacity, as shown in Fig. 11. The relative errors between the calculated results from the formula and the experimental data are all less than 4%. Additionally, the Boussinesq assumption is introduced to calculate the density of the crude oil (Eq. (24)), thereby improving the efficiency of numerical calculations.

$$\mu = \begin{cases} e^{4.74059-0.02231\times T_{\text{oil}}}, & 55\ ^\circ\text{C} < T_{\text{oil}} < 70\ ^\circ\text{C} \\ e^{9.38144-0.11057\times T_{\text{oil}}}, & 44\ ^\circ\text{C} < T_{\text{oil}} < 55\ ^\circ\text{C} \\ e^{(9.77424-0.10437)\times T_{\text{oil}}} \times \gamma^{0.93771-0.00489\times T_{\text{oil}}}, & 37\ ^\circ\text{C} < T_{\text{oil}} < 44\ ^\circ\text{C} \\ \dfrac{e^{(7.32342-0.16486\times T_{\text{oil}})}}{\gamma} + e^{19.69873-0.32904\times T_{\text{oil}}} \times \gamma^{-0.87266+0.04865\times T_{\text{oil}}}, & 20\ ^\circ\text{C} < T_{\text{oil}} < 37\ ^\circ\text{C} \end{cases} \tag{22}$$

$$c_{p_0} = A_1 + B_1 T_0 + C_1 {T_0}^2 + D_1 {T_0}^3 + E_1 {T_0}^4 + F_1 {T_0}^5, \quad 10\ ^\circ\text{C} < T_0 < 70\ ^\circ\text{C} \tag{23}$$

The values of A_1, B_1, C_1, D_1, E_1, F_1 are as follows: 2337.65332, 92.92462, −0.96629, −0.06914, 0.00155, −0.0000086779.

$$\rho_0 = \rho_{20}\left[1 - \beta(T_{\text{oil}} - 20)\right] \tag{24}$$

Water and two types of nanofluids with water as the base liquid were selected as the heat transfer fluid. The thermophysical properties of the nanofluids were estimated using the Maxwell

Table 1
Thermal physical properties of the heat transfer fluid.

Heat transfer fluid	Density, kg/m^3	Specific heat capacity, J/(kg·K)	Thermal conductivity, W/(m·K)
Water	998.2	4182	0.6
CuO-water nanofluid	1548.2	3815	0.774
Graphene-water nanofluid	1020	3800	0.758

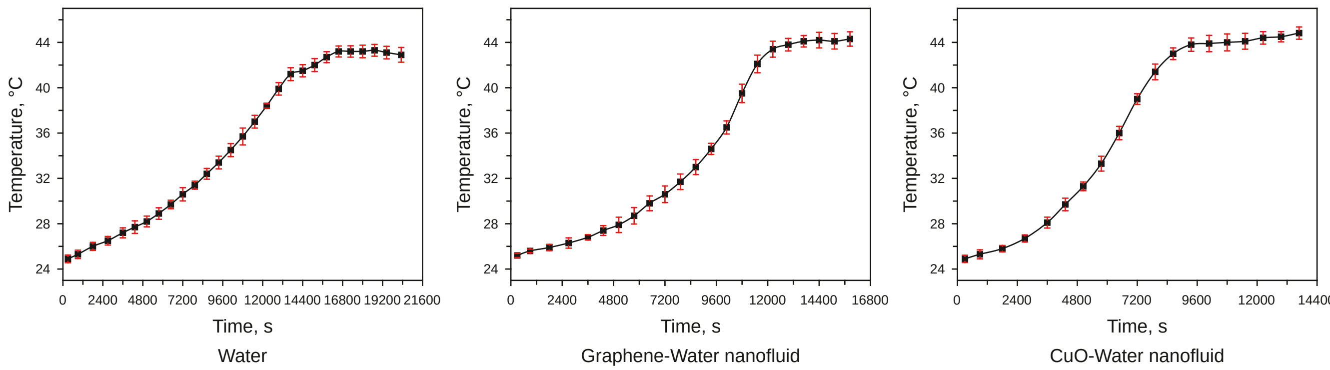

Fig. 12. Temperature variation at Point C-5 under different heat transfer fluids.

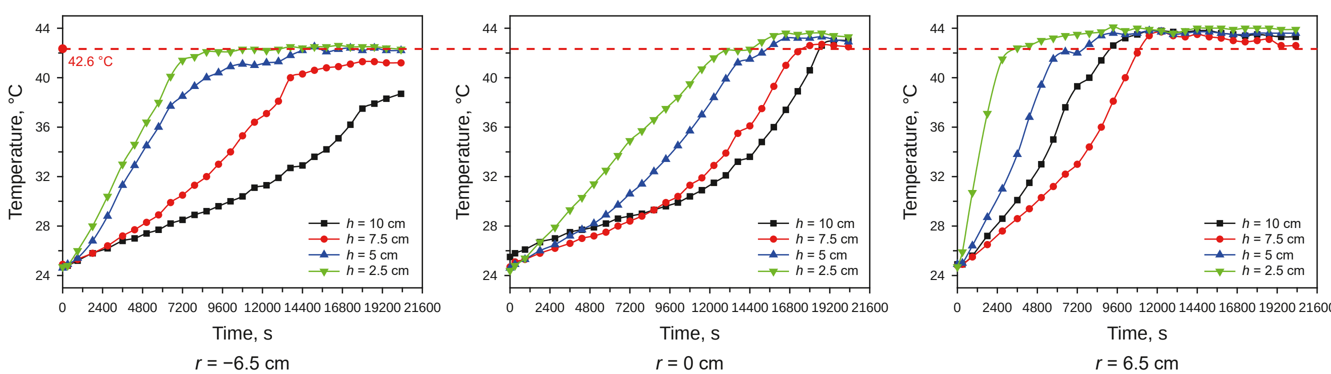

Fig. 13. Temperature changes at different points (with water as heat transfer fluid).

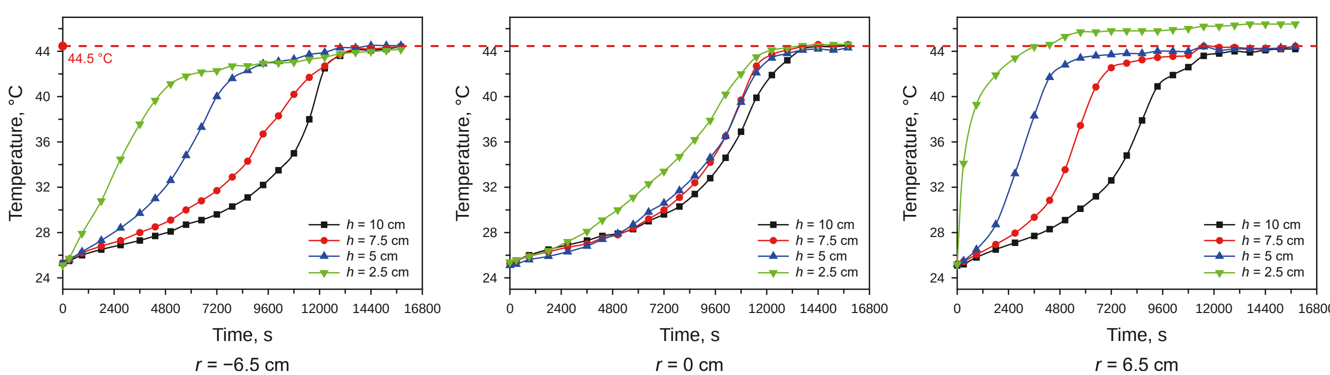

Fig. 14. Temperature changes at different points (with graphene-water nanofluid as heat transfer fluid).

model and related approaches (Hu et al., 2024). The thermo-physical parameters of the heat transfer fluid are shown in Table 1.

2.4. Temperature field variation pattern

2.4.1. Experimental results

This study conducted two independent replicate experiments, and the relative errors between them were calculated. Selected results are presented in Fig. 12. The calculated mean relative error was 5.95%, with all individual relative errors remaining within 10%. These results confirm the reliability and repeatability of the experimental results. The experimental results are shown in Figs. 13–19.

Regardless of the type of fluid used, a distinct axial temperature stratification phenomenon is observed (Figs. 13–15). In the initial heating stage (first 0.5 h), the temperature at the bottom (h = 2.5

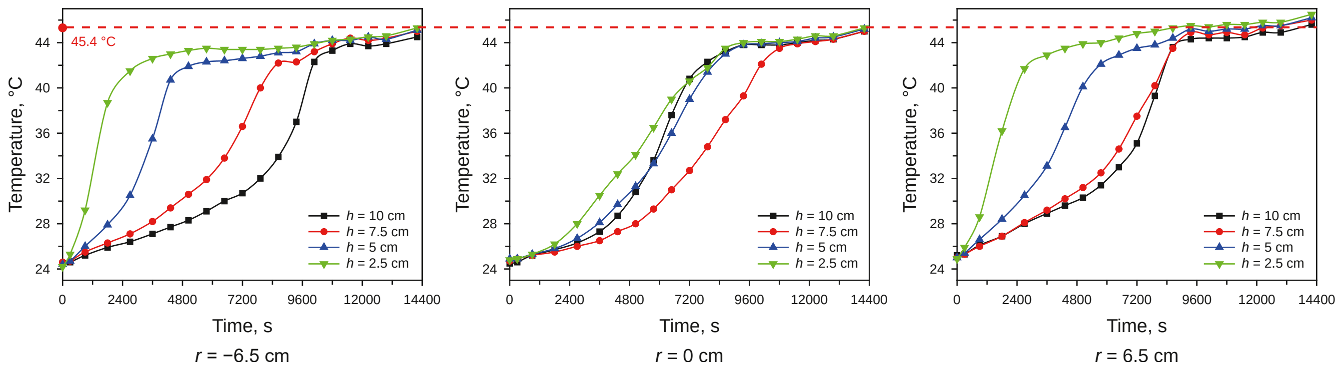

Fig. 15. Temperature changes at different points (with CuO-water nanofluid as heat transfer fluid).

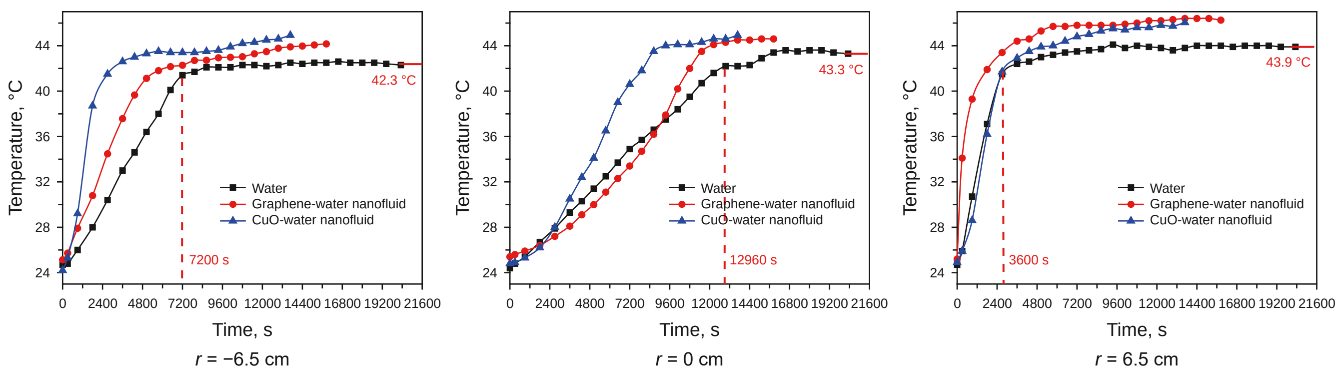

Fig. 16. Temperature at radial positions under $h = 2.5$ cm with different heat transfer fluids.

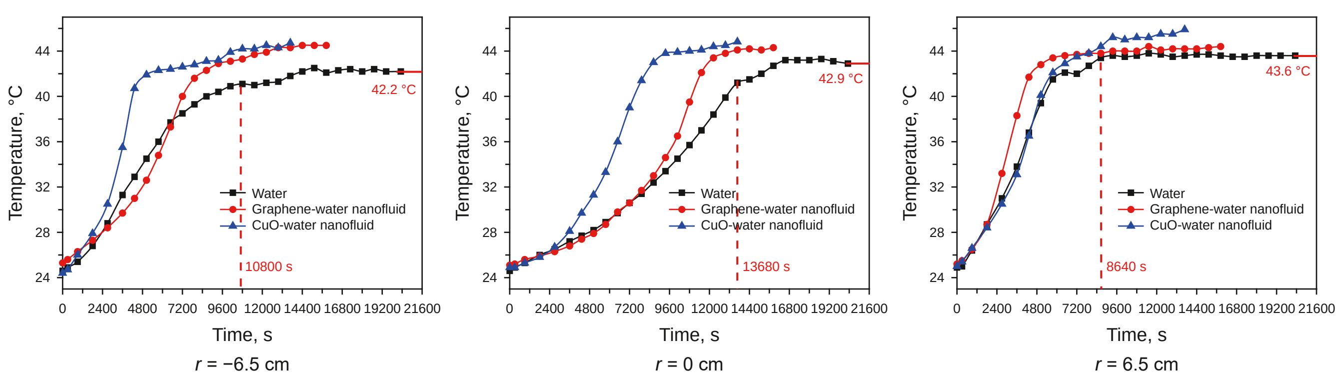

Fig. 17. Temperature at radial positions under $h = 5$ cm with different heat transfer fluids.

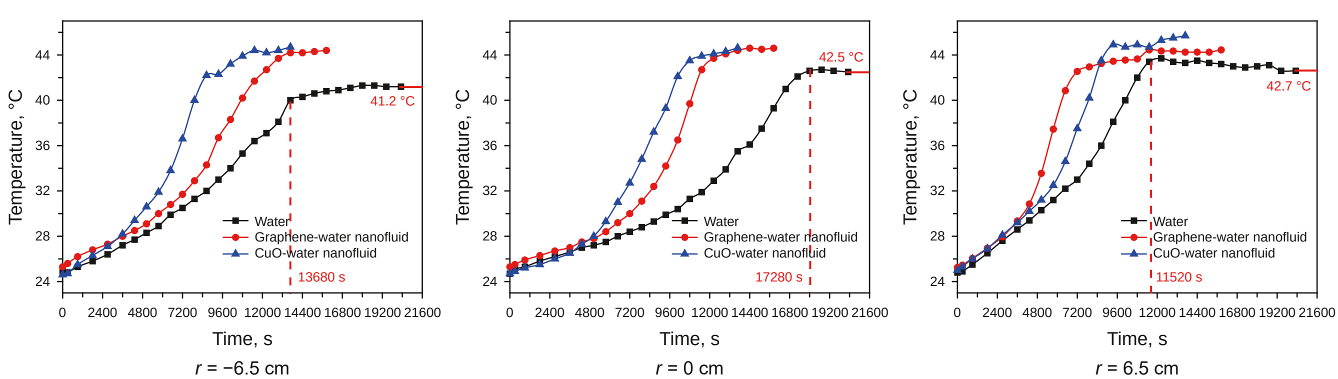

Fig. 18. Temperature at radial positions under $h = 7.5$ cm with different heat transfer fluids.

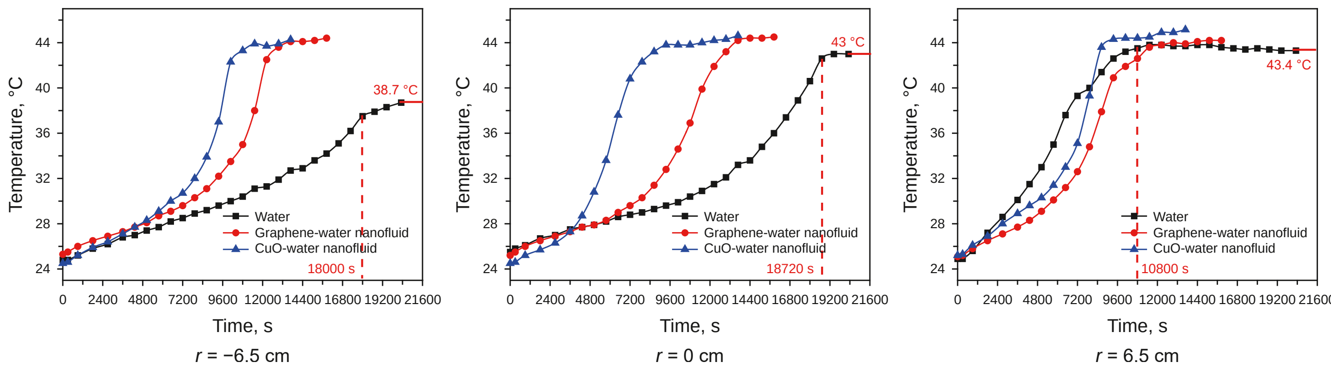

Fig. 19. Temperature at radial positions under h = 10 cm with different heat transfer fluids.

cm) rises rapidly, while that at the top (h = 10 cm) rises slowly, with a maximum temperature difference of 12.9 °C and an axial standard deviation of up to 5.38 °C between them. This is because the heat source is located at the bottom, and the heat is transferred upward through natural convection, resulting in the formation of a high-temperature zone at the bottom first, and then the top begins to heat up due to the thermal buoyancy effect. When using nanofluid (especially CuO-water nanofluid), the heating rate at the top position increased by approximately 66% compared to that when using water (h = 10 cm curves in Figs. 13 and 15 show heating rates of 5.17 °C/h for the CuO-water nanofluid and 3.11 °C/h for water). This indicates that the nanofluid enhance natural convection heat transfer and accelerate the transfer of heat to the top. At the same axial height (such as h = 2.5 cm), the temperature at the radial position r = 6.5 cm is significantly higher than that at r = 0 cm and r = −6.5 cm. This is because r = 6.5 cm is close to the inlet of the heating tube, and the heat transfer fluid temperature is higher, resulting in a greater heat exchange intensity. After 2 h of heating, a temperature difference of 2.5 °C was observed between r = 6.5 cm and r = −6.5 cm when using water as the heat transfer fluid (Fig. 13). In contrast, when using the CuO-water nanofluid, this temperature difference was reduced to 1.3 °C. Concurrently, the standard deviation of the radial temperature decreased from 3.66 °C for water to 1.75 °C for the CuO-water nanofluid. This demonstrates that the use of the nanofluid for heating results in a more uniform radial temperature distribution, yielding a temperature uniformity factor of 0.91. The CuO-water nanofluid exhibited the fastest temperature rise rate at all positions (Fig. 15), especially at the bottom measurement point (h = 2.5 cm), with its heating rate being 32% higher than that of water. This is because the CuO-water nanofluid has a higher thermal conductivity and moderate specific heat capacity, optimizing the balance between thermal diffusion and heat capacity. Temperature measurement points at different locations all showed an upward trend over time. During the initial stage of the experiment, the temperature rose relatively quickly, but it gradually slowed down as time passed, and finally stabilized. However, the thermal lag time of nanofluid is approximately 15% shorter than that of wate. This is because their higher thermal diffusivity speeds up the establishment of the system's thermal equilibrium.

By comparing the heating effects of different heat transfer fluid (Figs. 16–19), it can be seen that the heating effect of water-based nanofluids is superior to that of pure water. The heating rate is 5.24 °C/h (CuO) and 4.36 °C/h (graphene), which were higher than that of water (3.26 °C/h). However, both eventually stabilize, and the oil temperature at the corresponding position is also higher within the same time period. As shown in Fig. 17, at r = 0 cm and h = 5 cm (t = 3 h), the oil temperatures using CuO-water nanofluid and graphene-water nanofluid are 43.9 and 36.5 °C, respectively. Compared with heating with water, the temperature has significantly increased by 27.2% and 5.7%. This indicates that nanofluid can improve the heat transfer performance. The essence of this includes two aspects: first, the nanoparticles in the fluid will undergo irregular Brownian motion, constantly colliding with the surrounding fluid molecules, thereby intensifying the energy transfer within the fluid; second, the high thermal conductivity of nanofluid enhances heat transfer. This is also consistent with the numerical simulation results in the following text. Quantitatively, the CuO-water nanofluid yielded the most pronounced increase in oil temperature, indicating superior heating performance, followed by the graphene-water nanofluid.

2.4.2. *Temperature field comparison of different crude oil types*

To validate the universality of the heat transfer enhancement effect of nanofluids and to investigate the influence of crude oil physical properties on the heating process, this study selected Hulunbuir crude oil, which has a lower gel point and wax content, for comparison with Daqing crude oil. The temperature field evolution of the two crude oils under identical heating conditions (both using CuO-water nanofluid as the heat transfer fluid, at a room temperature of 19 ± 0.5 °C) is shown in Figs. 20–23.

The comparative results from Figs. 20–23 demonstrate that the CuO-water nanofluid significantly enhances heat transfer in both types of crude oil with distinct properties. The heating rates at all monitored points were substantially higher than the base case using water. This validates that the mechanism of nanofluid, through enhancing thermal conductivity and promoting fluid disturbance, thereby intensifying natural convection, is not limited to a specific crude oil, thus exhibiting broad applicability. Although the heating rate of Hulunbuir crude oil is largely comparable to that of Daqing crude oil, its ultimate equilibrium temperature is lower. This difference is primarily attributed to their distinct thermophysical properties. On one hand, the lower gel point and wax content of Hulunbuir crude oil result in diminished viscosity and improved fluidity, which significantly enhances the intensity and efficiency of natural convection within the tank, allowing the heat transfer enhancement effect of the nanofluid to manifest more rapidly. On the other hand, as the system approaches thermal equilibrium during heating, the heat input balances with the heat dissipated to the environment. At this point, due to the relatively good fluidity of the Hulunbuir crude oil, convective heat transfer at the top and along the walls is more intense, leading to increased heat dissipation loss. In contrast, the Daqing crude oil has not yet fully melted, with a large amount of gelled oil still present near the wall, resulting in weaker convective heat transfer and relatively lower heat dissipation loss. This difference causes the ultimate equilibrium temperature achievable under the same

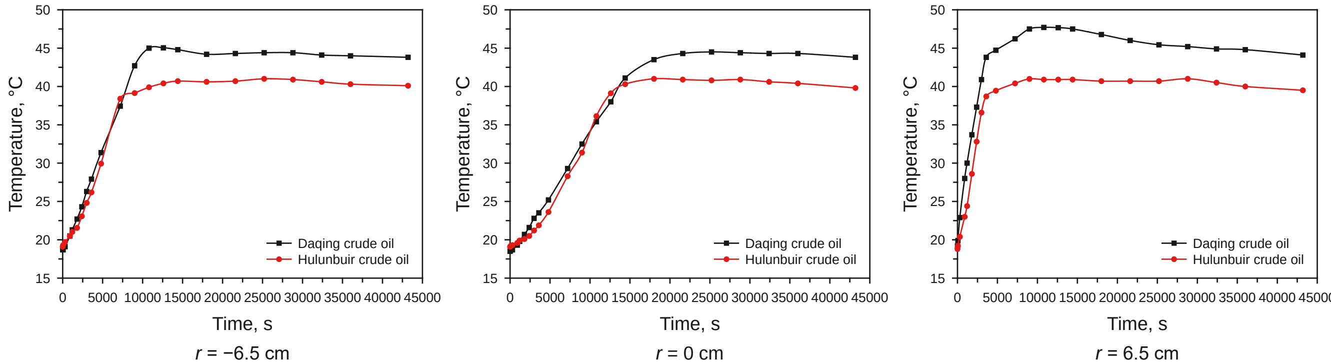

Fig. 20. Temperature at radial positions under $h = 2.5$ cm with different heat transfer fluids.

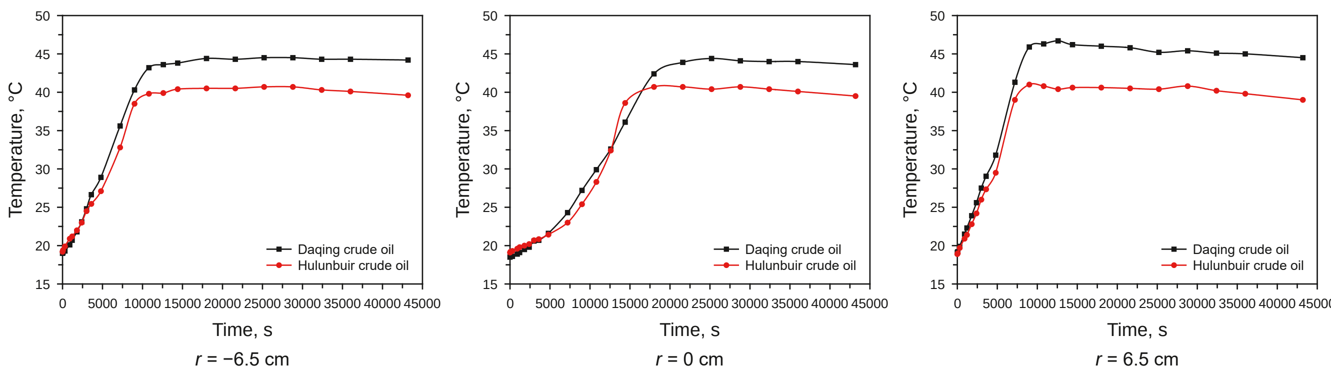

Fig. 21. Temperature at radial positions under $h = 5$ cm with different heat transfer fluids.

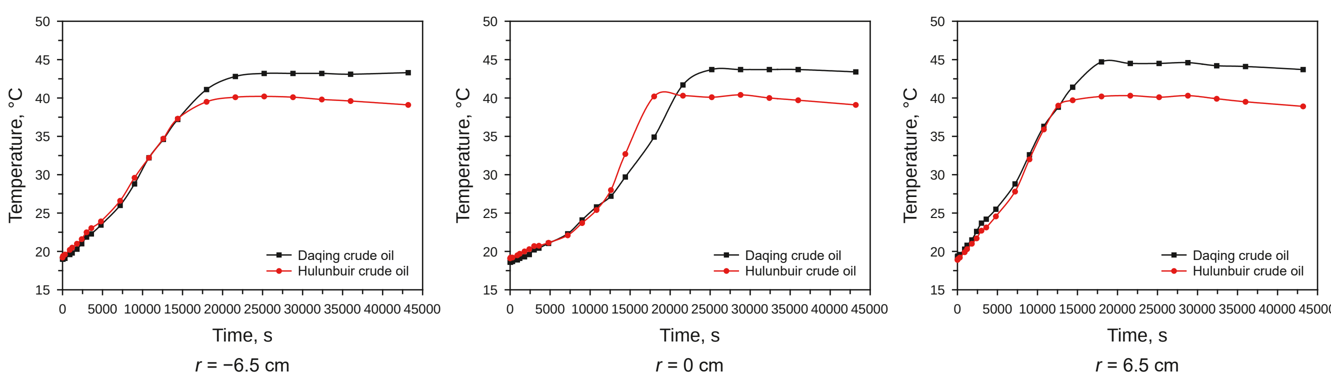

Fig. 22. Temperature at radial positions under $h = 7.5$ cm with different heat transfer fluids.

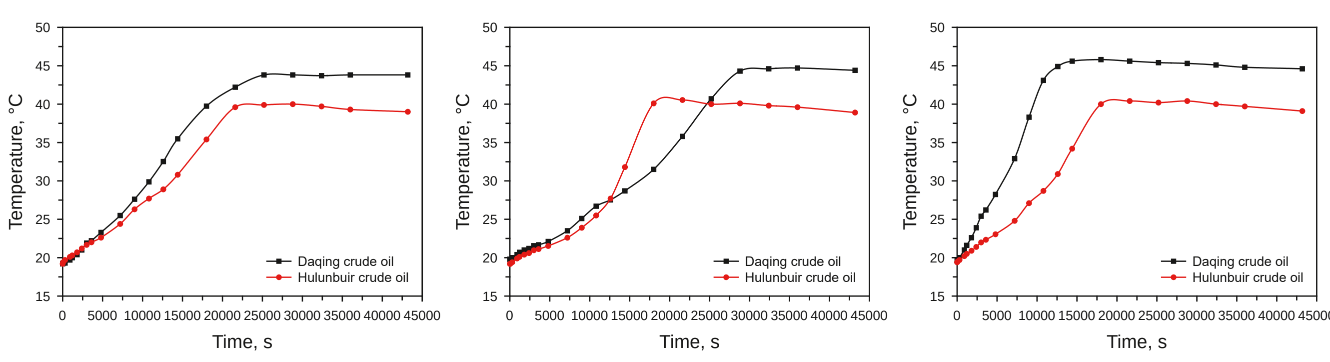

Fig. 23. Temperature at radial positions under $h = 10$ cm with different heat transfer fluids.

heating power to be lower for the Hulunbuir crude oil than for the Daqing crude oil.

Furthermore, Hulunbuir crude oil demonstrates superior radial temperature uniformity. As shown in Figs. 20–23, the heating rate at the central position ($r = 0$ cm) of Daqing crude oil consistently lagged behind both the peripheral positions ($r = \pm 6.5$ cm) and the corresponding locations in Hulunbuir crude oil. After 3 h of heating, at the same height ($h = 10$ cm), the radial temperature standard deviation of Daqing crude oil is 4.04 °C, while that of Hulunbuir crude oil is 1.64 °C, with a temperature uniformity factor of 0.88. This further indicates that the natural convection within the Hulunbuir crude oil is stronger, resulting in a more uniform temperature field distribution. After the experiment, it was observed that some gelled oil remained in areas of the Daqing crude oil far from the heating tube, and the temperature of this congealed oil was lower than that at corresponding locations in the Hulunbuir crude oil. This suggests that the difference in average temperature between Daqing crude oil and Hulunbuir crude oil is actually smaller than the temperature difference shown in Figs. 20–23.

2.4.3. Temperature field during intermittent heating mode

To evaluate the impact of alternative heating modes on the internal temperature field uniformity and heat transfer process of the device, this study introduced intermittent heating experiments. Fig. 24 shows the temperature evolution curves at three characteristic positions ($r = -6.5$, 0, 6.5 cm) during the periodic "heating-intermittent" cycles. Compared with the continuous heating mode (Figs. 20–23), the final average temperature under intermittent heating was only 38.06 °C, representing a reduction of 13.3%, while different radial positions exhibited regular and differentiated responses.

The peak temperature at $r = 6.5$ cm remains stable throughout the intermittent cycles. This region is closest to the high-temperature inlet of the heating tube and is the direct action zone of the heat source. The nanofluid, leveraging its high thermal conductivity, ensures efficient and stable heat transfer from the tube wall to the fluid, enabling this region to rapidly return to the high temperature level of the previous cycle during each heating phase. Its thermal behavior is primarily controlled by the external heat source.

The peak temperature at $r = -6.5$ cm shows a gradually decreasing trend (41.73 °C→37.68 °C→34.61 °C). This phenomenon results from the combined effects of heat source location and internal flow dynamics. On one hand, this position is situated near the outlet of the heating tube, where it receives nanofluid that has already undergone heat exchange, resulting in an initially weaker thermal driving potential and consequently a relatively sluggish thermal response. On the other hand, during the heating intermittence periods, natural convection driven by internal temperature differences within the system becomes fully developed. The combined action of these two effects leads to a successive decrease in the initial temperature of this region before each reheating cycle, ultimately manifesting as the observed attenuation of peak temperature.

Conversely, the peak temperature at $r = 0$ cm exhibits a slight gradual increase over successive cycles. During the heating phase, heat is transferred to various parts of the setup through convection, while during the intermittent phase, the natural convection enhanced by the nanofluid acts as an "internal mixer" delivering heat toward the cooler central region. With its periodic on-off operation, intermittent heating effectively stimulates and utilizes the natural convection within the system, achieving a redistribution of heat from the near-wall area toward the central zone.

2.5. Comparison of experiments and simulations

2.5.1. Experimental validation

Compared with the experimental and simulation results (Fig. 25), the time course of the average temperature of the crude oil has a high degree of consistency. After heating for 3.9 h, the heating rates measured by the experiment and simulation were 5.21 and 4.98 °C/h respectively, with a relative deviation of 4.61%. The temperature change trends at each monitoring point were basically consistent, with the maximum relative error of 4.58% and the average relative error of 2.62%, which was relatively close. This fully proves that the adopted mathematical model, grid division strategy and solution algorithm are all applicable to the simulation of the phase change heat transfer process of waxy crude oil, laying a foundation for subsequent research.

It should be noted that this experiment employs a small-scale model, which differs significantly in size from actual size oil storage tanks. This discrepancy may introduce certain scaling effects, such as more pronounced heat loss through the sidewalls and liquid surface, as well as differences in internal natural convection and gel-melting behavior. Therefore, the primary objective of this small-scale experiment is not to directly and quantitatively replicate the actual conditions of an actual size tank, but rather to: (1) qualitatively reveal the core physical mechanisms of nanofluid as heat transfer fluid in a structurally similar but reduced-scale apparatus; (2) provide key experimental data for validating the accuracy and reliability of the subsequent numerical model, use the experimentally validated numerical model to further simulate and predict the behavior in actual size tanks, thus ensuring effective extrapolation of the conclusions to engineering scales.

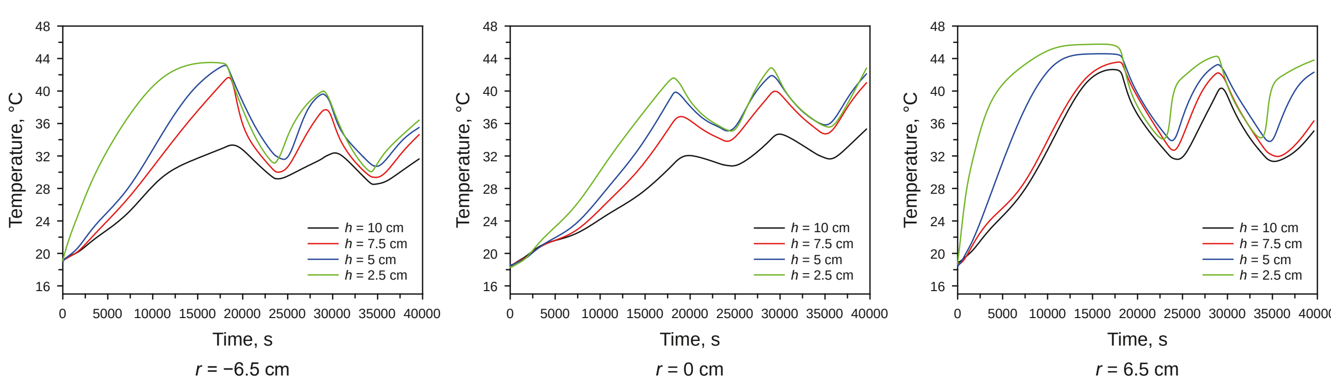

Fig. 24. Temperature changes under intermittent heating mode.

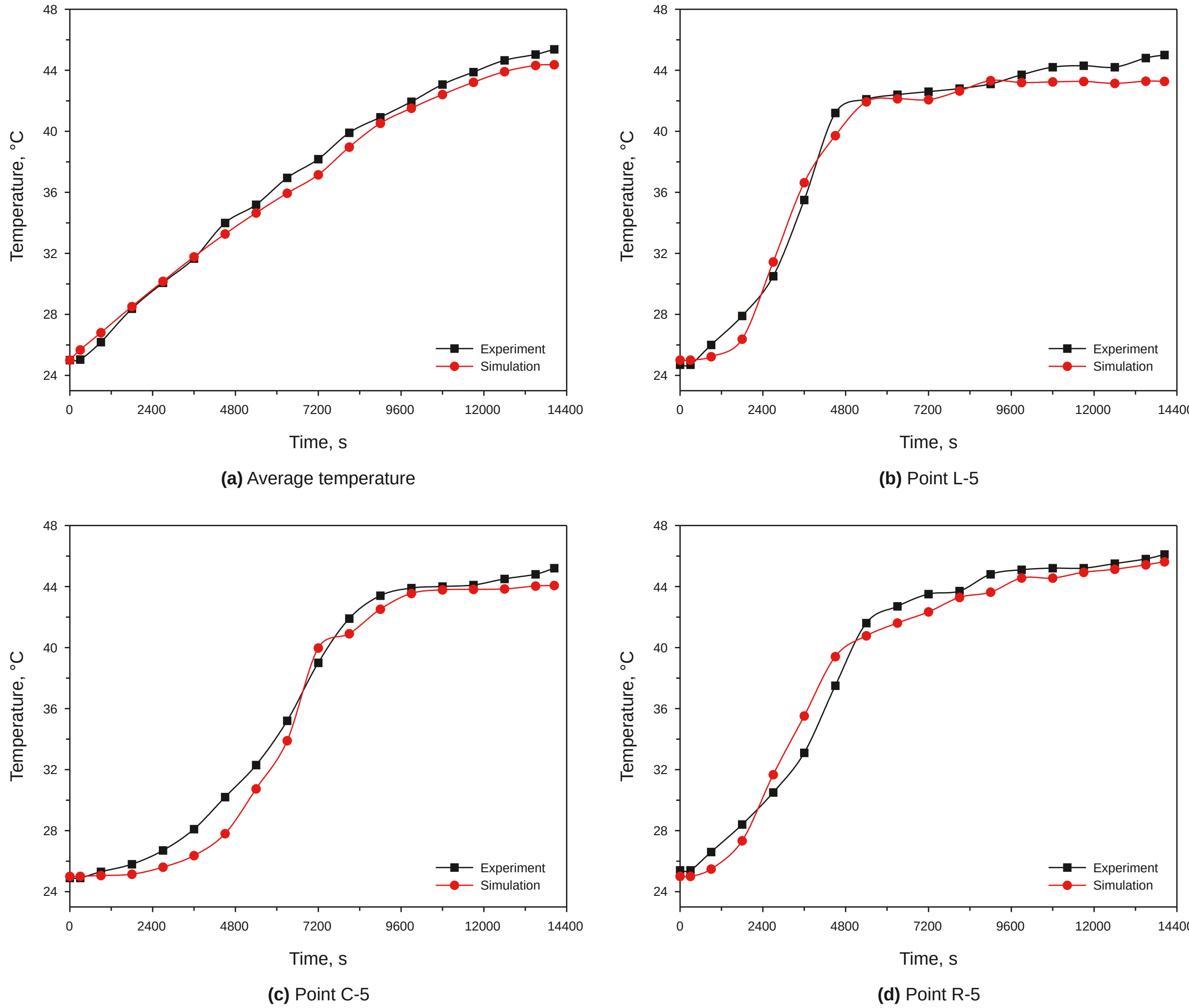

Fig. 25. Temperature changes at different measurement points.

2.5.2. Gel-sol transition rules

During the experiment, the gel-sol transitions of the waxy crude oil at different times are shown in Figs. 26–29.

Fig. 26 clearly shows that after 15 min of heating, the crude oil in gel state began to transform into sol state and "flow" on the liquid surface. When using nanofluid, especially CuO-water nanofluid, the area where the crude oil around the heating tube melts (the area marked in red by the dotted line) is much larger than in the case of using water. Water only causes a small amount of crude oil near the heating tube to melt, while the nanofluid has formed a significant "dissolving cavity", and the gradually expanding transitional zone around the periphery is also more extensive. This indicates that in the initial stage of heating, the nanofluid can transfer heat to the crude oil at a higher rate, accelerating the transition of the gelled oil. After 1 h of heating (Fig. 27), the difference further expands. When heating with CuO-water nanofluid, the melting area has formed a widespread natural convection pattern, with the hot crude oil near the side wall and the bottom near the heating tube area surging upward, driving the heat to be transferred to the top, and the transitional zone increases; graphene-water nanofluid comes next. However, the range of solubility corresponding to the use of water is still significantly limited, and the convection intensity is relatively weak. This indicates that the nanofluid, by enhancing heat transfer, not only accelerates the transition of gel-sol, but also significantly promotes the development of natural convection within the crude oil, thereby facilitating the transfer of heat. From Figs. 28 and 29, it can be observed that when the heating was carried out using the CuO-water nanofluid with the strongest heating effect (for 3.9 h), a portion of the crude oil had completely transformed into sol state and exhibited good fluidity. Another part is still in a transitional state. A small portion of the crude oil, due to its location far away from the heating tube, remains in gel state.

In order to achieve approximately the same global temperature within the device, it takes 5.6 h to heat with water, and the transitional and gel regions in its final state still account for a certain proportion; graphene-water nanofluid also requires 4.2 h, but it is still significantly superior to water (the time is shortened by 25%), although its transitional regions are fewer than water, they are still more than those of CuO-water nanofluid. The heating efficiency of CuO-water nanofluid is the highest, and the time taken is the shortest (3.9 h). This indicates that nanofluid, especially CuO-water nanofluid, not only accelerate the melting of the oil but also effectively promote the transition of crude oil from gel to transitional state to sol. Based on the above experimental results,

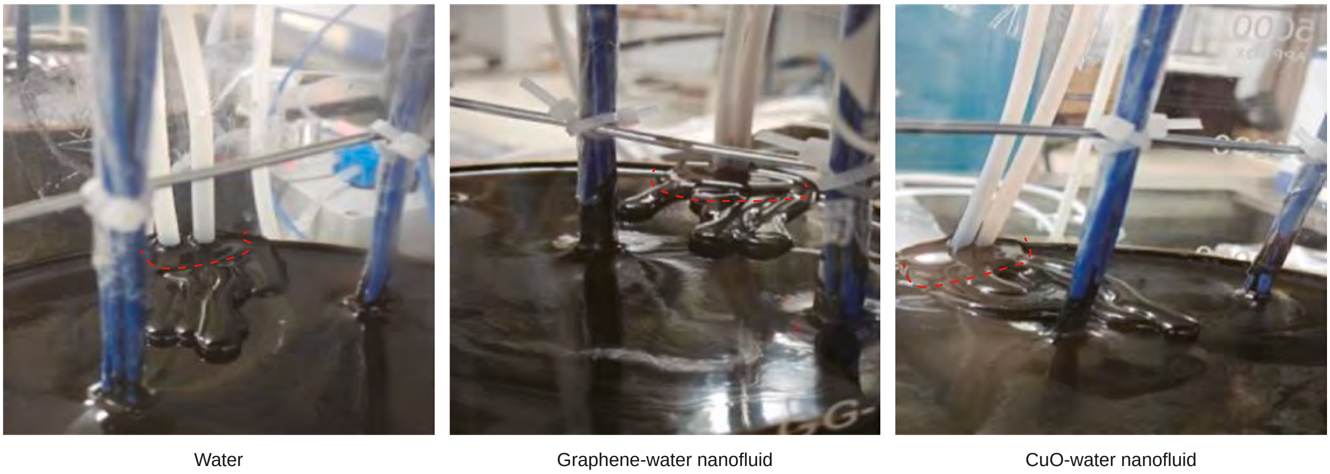

Fig. 26. Crude oil heated for 15 min using different heat transfer fluids.

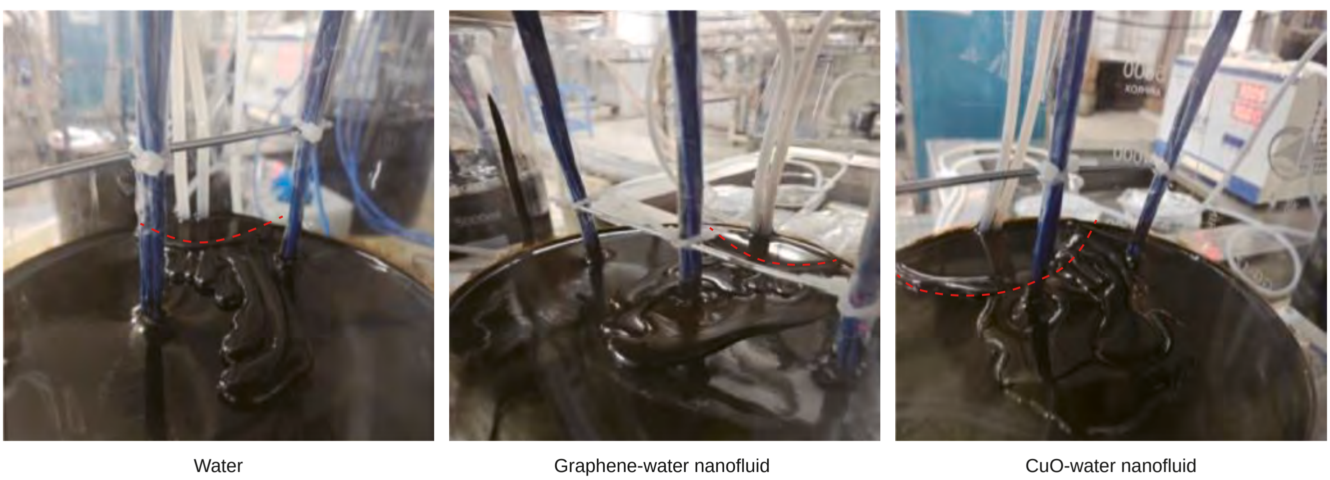

Fig. 27. Crude oil heated for 1 h using different heat transfer fluids.

Fig. 28. Crude oil heated for 3.9 h using different heat transfer fluids (using CuO-water nanofluid completed).

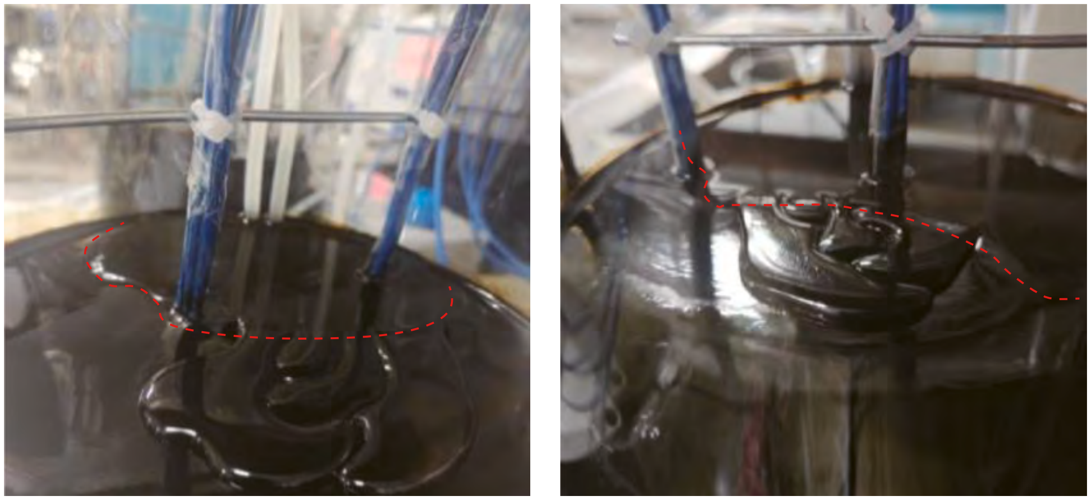

Fig. 29. Crude oil after being heated with water/graphene-water nanofluid.

the evolution of crude oil from gel to sol can be divided into four stages as shown in Fig. 30, and the synchronous simulation results are also listed as shown in Fig. 31.

A comparison between Figs. 30 and 31 reveals a high degree of consistency between the simulated and experimental results regarding the gel-sol transition process of the waxy crude oil. Fig. 31 shows the evolution process of the temperature field at the $X = 0$ section along the heating tube inlet direction when heated by CuO-water nanofluid. In the initial heating stage (5–15 min), heat transfer is dominated by conduction, and the high-temperature zone is limited to the vicinity of the heating tube wall and decreases radially outward along the tube wall in a concentric circular pattern, forming a typical "thermal shell" structure. At this point, most of the crude oil remains in a low-temperature state, with a significant overall temperature gradient and no large-scale organized flow has yet formed. During this stage, the nanofluid rapidly raises the temperature of the crude oil near the heat source due to its high thermal conductivity. Heat for the middle stage (30 min–1 hour). As the heating progresses, the density of the crude oil near the heating tube decreases due to heating. Driven by the buoyancy force, it begins to move upwards. The crude oil undergoes natural convection, and the hot crude oil detaches from the heating tube wall, forming clear, upward-moving thermal plume. The amount of crude oil in gel state has significantly increased. During the later stage of heating (2–3.9 h), due to the effect of natural convection, most of the crude oil transforms into the transition state and the sol state. Only a limited low-temperature area exists in the upper part. The overall results of the numerical simulation are consistent with the experimental analysis conclusion in Fig. 30. There may be some errors in the local areas. In addition, the range of the melting area of the crude oil liquid surface at the final heating moment (the area indicated by the dotted line box) is also relatively close to the area range recorded in the experiment.

3. Numerical simulation of the actual size of the oil storage tank

Further, the above-mentioned validated method was applied to conduct a simulation study on the tubular heating process of actual size oil storage tank under the influence of nanofluid.

3.1. Construction of the computational domain

Taking a floating roof oil storage tank with a volume of 1000 m^3 and equipped with a tubular heating system as the research object, the tank has a diameter of 12 m and a liquid level height of 5 m. Fig. 32 shows the longitudinal section view of the floating roof tank. In the tank, spiral heating tubes are used, and heat transfer fluid flows inside the heating tubes. The inlet and outlet extend outside

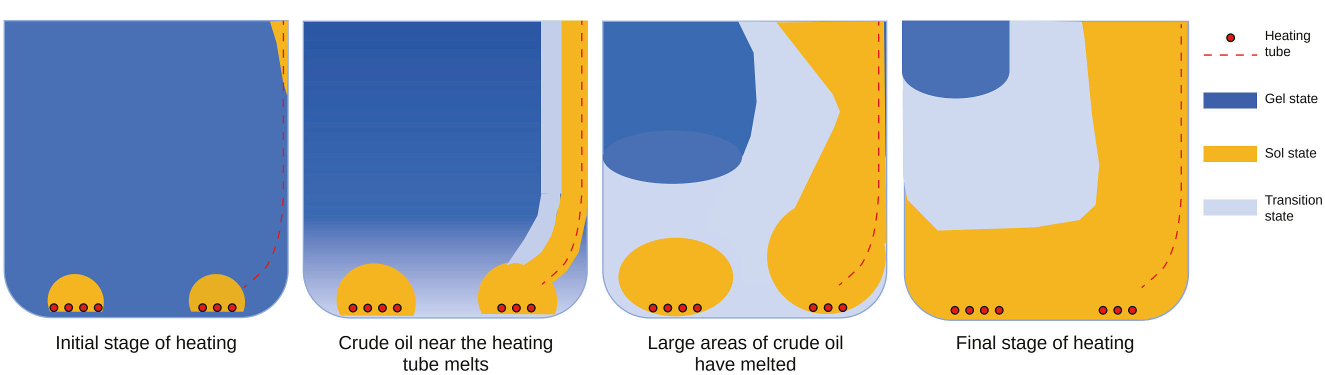

Fig. 30. Gel-sol transition process of crude oil (at the cross-section of $X = 0$ along the heating tube inlet direction).

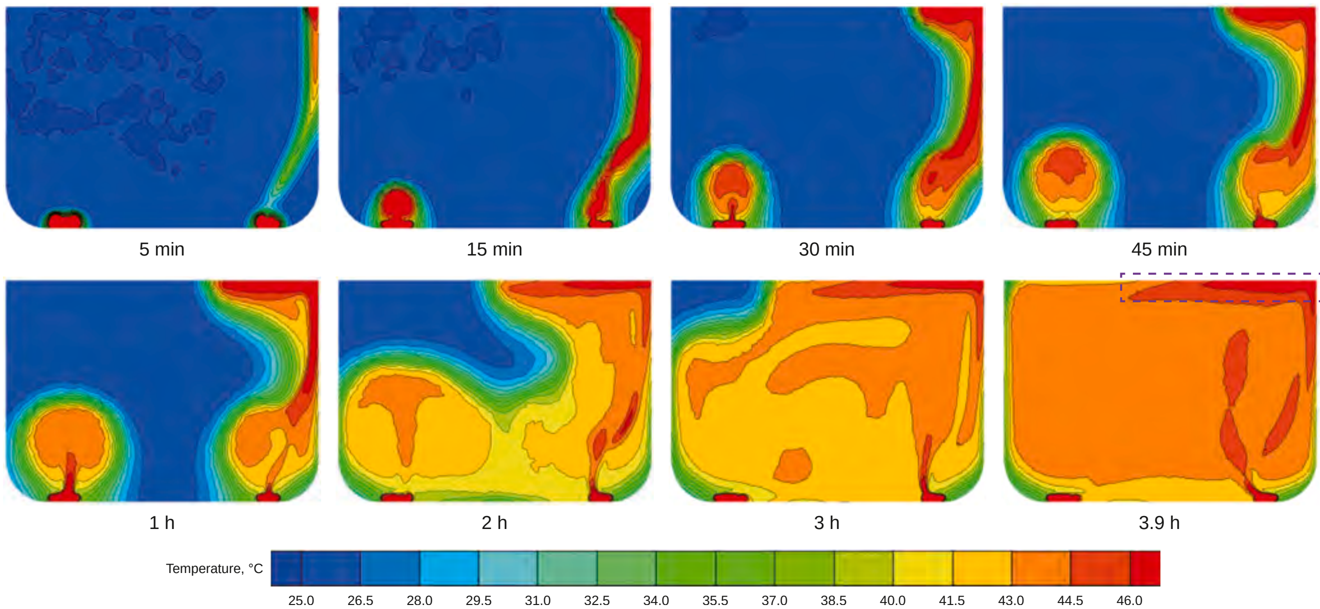

Fig. 31. Evolution of the temperature field at the cross-section of $X = 0$ along the heating tube inlet direction (CuO-water nanofluid) (red/orange: sol, blue: gel, yellow: transition state).

the tank body, with the maximum diameter of 10.9 m and the minimum diameter of 0.7 m. The inner diameter of the heating tubes is 60 mm, the total length is 91 m, and the total heating area is 18.6 m^2. The heating tubes are horizontally arranged, with a distance of 1 m from the bottom of the tank. The heat transfer coefficient between the tank top, tank wall and the environment is 32.12 W/(m^2·K). The boundary thickness of the tank top (representing the air layer and the floating roof) is 0.7 m, the boundary thickness of the tank wall (representing the insulation layer) is 0.08 m, and the thickness of the soil layer in contact with the bottom of the tank is 12.5 m.

While ensuring the accuracy of the numerical simulation, the computational efficiency was improved by simplifying the storage tank structure. The main structure of the storage tank was retained, and the tank top, tank wall, and tank bottom were defined as the boundary of the calculation domain. The thermal resistances of the soil layer at the bottom of the tank, the insulation layer on the tank wall, and the air layer at the top were considered. By using the method of given total thermal resistance, the structure of the tank top, tank wall, and tank bottom was simplified to a single-layer plate, thereby retaining the influence of the actual storage tank on the heat transfer characteristics of the internal crude oil. Based on relevant design standards and engineering data, a heating tube model that conforms to engineering reality was established (Fig. 33(b)). To be as close as possible to the engineering reality, a three-dimensional modeling method was adopted to construct the model of the calculation domain, as shown in Fig. 33(a). The material property parameters of the boundary materials are listed in Table 2.

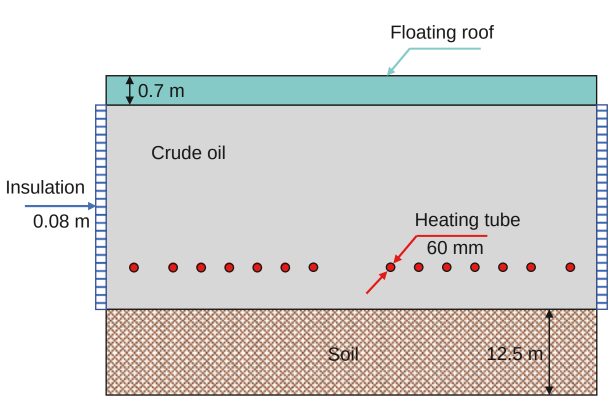

Fig. 32. Floating roof oil storage tank equipped with tubular heating system.

3.2. Mathematical model

For the tubular heating process of actual size storage tank, the numerical simulation adopts the same basic control equations as in Section 2.2, as well as the boundary conditions inside and outside the heating tubes. Some of the boundary conditions have been set according to the actual working conditions.

3.2.1. Boundary conditions

(1) The top and walls of the actual storage tank are exposed to the air. Therefore, in the numerical simulation, the top and walls of the tank are defined as the third boundary conditions. At the same time, the thermal resistances of the air layer on the top and the insulation layer on the walls are considered. The ambient temperature and convective heat transfer coefficient are given:

$$h = H_{\text{tank}}, 0 \le r \le R_{\text{tank}}, -\lambda_{\text{topwall}} \frac{\partial T_{\text{topwall}}}{\partial h} = h_{\text{topwall}} \left(T_{\text{topwall}} - T_{\text{air}} \right), u_{\text{topwall}} = 0 \tag{25}$$

$$0 \le h \le H_{\text{tank}}, r = R_{\text{tank}}, -\lambda_{\text{sidewall}} \frac{\partial T_{\text{sidewall}}}{\partial h} = h_{\text{sidewall}} (T_{\text{sidewall}} - T_{\text{air}}), u_{\text{sidewall}} = 0 \tag{26}$$

(2) The bottom of the storage tank is located at a depth of 12.5 m in the soil. The temperature of the soil at this depth

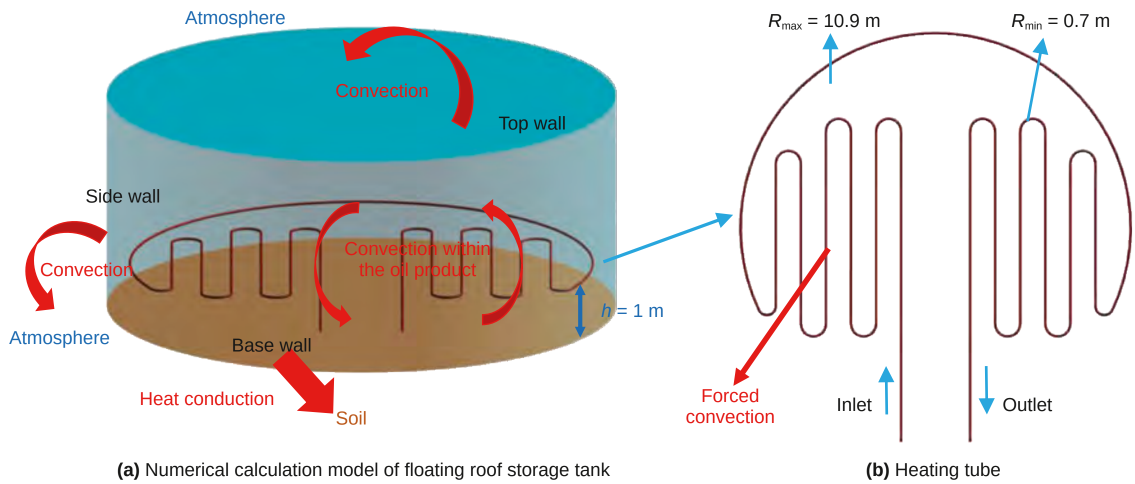

Fig. 33. Computational domain of the numerical simulation.

remains constant, and the bottom of the tank is defined as the first boundary condition:

$$h=0, 0\le r\le R_{\text{tank}}, T_{\text{soil}}=T_{\text{basewall}}, u_{\text{basewall}}=0 \tag{27}$$

3.2.2. Initial condition

In the initial state of the tubular heating process, the crude oil in the storage tank is stationary and the temperature distribution is uniform:

$$T_{\text{oil}}(t=0,r,\phi,h)=T_0, u(t=0,r,\phi,h)=u_0 \tag{28}$$

3.3. Numerical method

3.3.1. Discretization of the computational domain

Based on the structural characteristics of the inner and outer sub-regions of the heating tube, while ensuring the accuracy of the calculation, the non-structured grid partitioning method is adopted to discretize the calculation domains of the two parts. The key challenge lies in the significant geometric scale difference between the computational domain of the heating tube and the computational domain of the crude oil. The computational domain of the heating tube requires a more refined mesh to capture the characteristics of the heat transfer boundary layer, while the computational domain of the crude oil requires an appropriate mesh size to control the computational scale. Therefore, using polyhedral honeycomb mesh division can largely reduce the size difference between the inside and outside of the heating tube, thereby improving the calculation accuracy. The grid system of the computational domain is shown in Fig. 34. For the boundaries of the computational domain with large velocity and temperature gradients, as well as the areas near the heating tubes where the temperature changes significantly, grid densification is required.

Table 2
Properties of boundary materials.

Boundary	Density, kg/m^3	Thermal conductivity, W/(m·K)	Specific heat capacity, J/(kg·K)
Top wall	1.225	1.05	1006
Side wall	60	0.055	800
Base wall	1600	1.74	1750

As shown in Fig. 34(c), the minimum grid size in the area near the heating tube is 10 mm. This minimum grid size expands at a growth rate of 1.2 times towards the top, bottom, and wall boundaries of the tank. The grid division is carried out in accordance with the above method, and the total number of grids is 3,603,466. The minimum and maximum grid sizes are 10 and 180 mm, respectively.

3.3.2. Discretization of the governing equations

For the natural convection and non-isothermal flow during the tubular heating process of crude oil storage tank, the finite volume method based on unstructured grids is adopted for discretization. The transient term is handled using a first-order fully implicit scheme. Although this scheme has a first-order time step difference, it is unconditionally stable and is suitable for long-term slow-evolution processes. It allows for the use of larger time steps, significantly improving computational efficiency. The viscous stress term and the heat conduction term in the momentum and energy equations are discretized using the second-order central difference (CDS) scheme to ensure the conservation and accuracy of the flux calculations. The convective term is discretized using the improved QUICK scheme to reduce numerical diffusion and more accurately capture the evolution of the heat plum. To accurately solve the pressure field and handle the buoyancy source term, the volume force weighted format is used for pressure interpolation, thereby enhancing the authenticity and stability of the buoyancy-driven flow field. At the same time, an alternating grid storage strategy is adopted to avoid non-physical oscillations caused by the decoupling of pressure and velocity. Finally, the SIMPLE algorithm was utilized to achieve the pressure-velocity coupling solution, thereby enhancing the computational stability and efficiency.

3.4. Validation procedure

3.4.1. Validation of grid independence

In order to eliminate the influence of different grid parameters on the simulation results, under the premise of using the same model, different grid parameters were designed for the simulation. By comparing the simulation results of different grids, the independence of the grids was verified, and the optimal grid was selected. The design schemes of different grids are shown in Table 3.

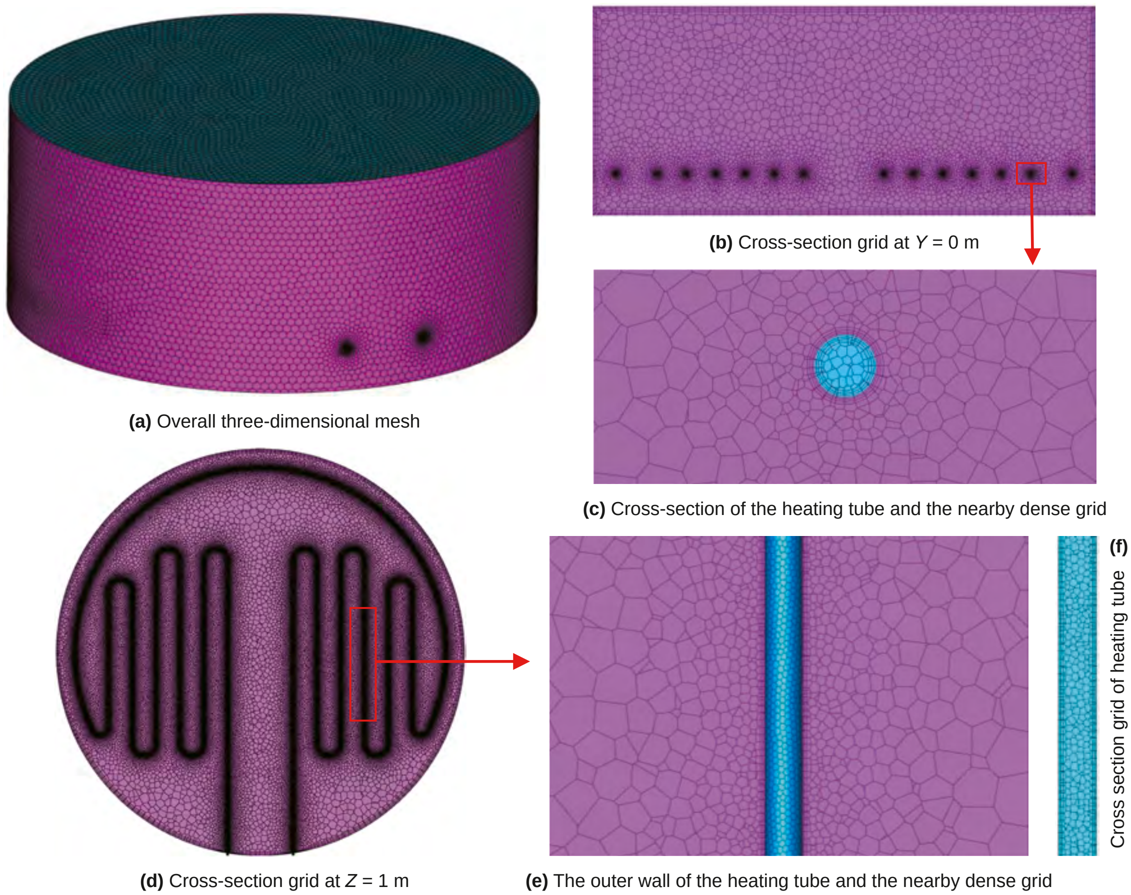

Fig. 34. Grid system of the numerical calculation domain.

Table 3
Different grid design schemes.

Grid	Minimum gird size, mm	Growth rate	The number of grids	Computational time, h
Grid 1	20	1.2	1,339,588	0.82
Grid 2	18	1.2	2,602,943	2.26
Grid 3	10	1.2	3,603,466	2.8
Grid 4	8	1.2	4,911,510	6.48

Under the same boundary conditions and time step, simulations of the 1-h tubular heating process were conducted for four different grids, and the *Nu* number on the surface of the heating tube was monitored (Fig. 35). The results show that although the calculation times of grids 1 and 2 are short, the Nu values are significantly smaller and there is a considerable deviation from grids 3 and 4. This indicates that these grids are too sparse and are unable to accurately capture the heat transfer behavior near the heating tube. The *Nu* values of grid 3 and grid 4 are close, indicating that both grids have achieved high accuracy. However, the calculation time of grid 4 is 3.68 h longer than that of grid 3. To balance the calculation efficiency and accuracy, grid 3 was ultimately selected for the subsequent simulation. Its grid division is shown in Fig. 34.

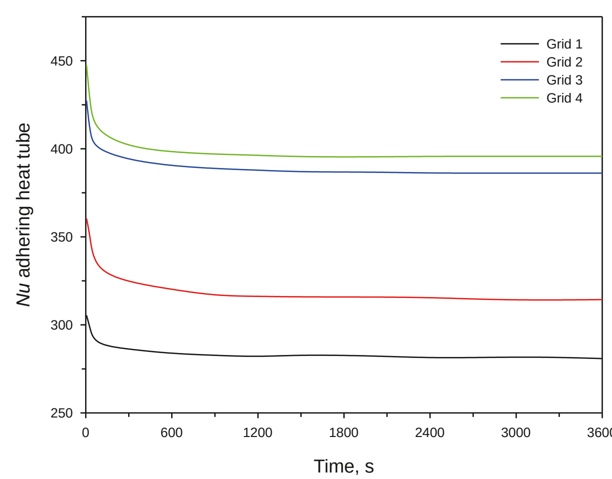

Fig. 35. Variation of surface *Nu* number with time for different grids.

3.4.2. Validation of algorithms and models

The validation of the algorithm and mathematical model was carried out based on the small-scale experimental results and corresponding numerical simulations described in Section 2.5. In this section, the relative deviation in heating rate between the indoor experiment and the corresponding simulation was found to be 4.61%, with a maximum relative error of 4.58% and an average relative error of 2.62%. The temperature variation trends at each monitoring point were essentially consistent, and the gel-sol transition process of the crude oil reflected in both the experiment and the simulation showed good agreement. These results fully demonstrate that the mathematical model, crude oil property characterization method, and solution algorithm employed in this study can accurately describe the phase change process of waxy crude oil and effectively reflect the enhanced heat transfer effect of the nanofluid.

However, considering the influence of scale effects, authors' group previously conducted temperature measurements of crude oil in an actual 100,000 m^3 storage tank (80 m in diameter) at the Daqing Oilfield in China (Yang et al., 2018). Six groups of test tubes were arranged near the inlet, at the center, in the gauge hatch, and at different radial positions to acquire the temperature distribution inside the tank, aiming to verify the model's applicability to large-scale tanks. Correspondingly, a physical model based on this actual tank was established, and numerical simulations were performed (Zhao et al., 2025b). The temperature variation trends at different heights along the central axis of the tank show general consistency. The maximum relative error between the simulated results and the measured temperatures is 7.64%, the minimum relative error is 2.85%, and the average relative error is 4.92%, indicating that the numerical model retains high predictive accuracy under full-scale conditions. Integrating the validation outcomes from both the small-scale experimental setup and the actual storage tank, the established mathematical model, numerical algorithms, and mesh strategy exhibit good applicability and reliability across different scales.

4. Actual size simulation results of the oil storage tank

4.1. Simulation cases

Based on the aforementioned physical model and mathematical model, a numerical simulation was conducted on the heat transfer process of crude oil under the condition of tubular heating. The initial temperature of the crude oil was uniformly set at 40 °C, the ambient temperature was −20 °C, the inlet temperature of the heating tube was maintained at 80 °C, and the heating time was all set to 5 h. Based on the differences in the heat transfer fluid, three cases were designed. The main parameters in the cases are shown in Table 4.

4.2. Simulation results using water as the heat transfer fluid

4.2.1. Simulation results of three-dimensional physical field

Fig. 36 shows the three-dimensional temperature and velocity field distribution within the storage tank after 5 h of heating when water is used as the heat transfer fluid. Two sets of cross-sections are selected in the figure: one is parallel to the heating tube (in the *y* direction), and the other is perpendicular to it (in the *x* direction). The simulation results show that the average temperature of the crude oil increased from the initial 40 to 40.44 °C. The overall temperature distribution was relatively uniform, but there were still significant temperature differences in some areas. The variance of the temperature across the entire area was 1.41 $°C^2$. The high-temperature areas are mainly located around the heating tubes, in the upper part of the storage tank, and near the inlet of the heating tubes; the low-temperature areas are concentrated below the heating tubes, especially in the area close to the bottom of the tank, with a temperature difference of approximately 0.5 °C compared to the central area. This difference is, on the one hand, due to the intense heating of the crude oil near the heating tube; on the other hand, it is because the heating tube is not evenly arranged, with a smaller heating area at the inlet side, resulting in a weaker effect. Furthermore, during the flow of the heat transfer fluid through the heating tube, it continuously releases heat to the crude oil. Its temperature decreases from 80 °C at the inlet to 64.3 °C at the outlet (Fig. 37), with an average temperature drop rate of 0.172 °C/m. As the heat transfer fluid advances along the tube, the temperature difference driving heat exchange with the external crude oil diminishes, leading to a corresponding reduction in local heating capacity.

Fig. 37 clearly shows the influence of the uneven distribution of heating tubes on the temperature field. Analyzing along the $y = 0$ section as the symmetry plane, it can be seen that the heating tubes are more densely distributed in the $y > 0$ region, resulting in an average oil temperature of 40.44 °C in this area, which is slightly higher than 40.43 °C in the $y < 0$ region. Although the average temperature difference between the two regions is relatively small, there are still significant temperature variations in some local areas. The influence of the temperature drop of the heat transfer fluid inside the heating tube on the temperature field can

Table 4
Conditions of simulation for different cases.

Case	Temperature at the inlet of heating tube, °C	Inlet flow rate, m/s	Heat transfer fluid	Initial temperature of crude oil, °C
Case 1	80	0.3	Water	40
Case 2	80	0.3	CuO-water nanofluid	40
Case 3	80	0.3	Graphene-water nanofluid	40

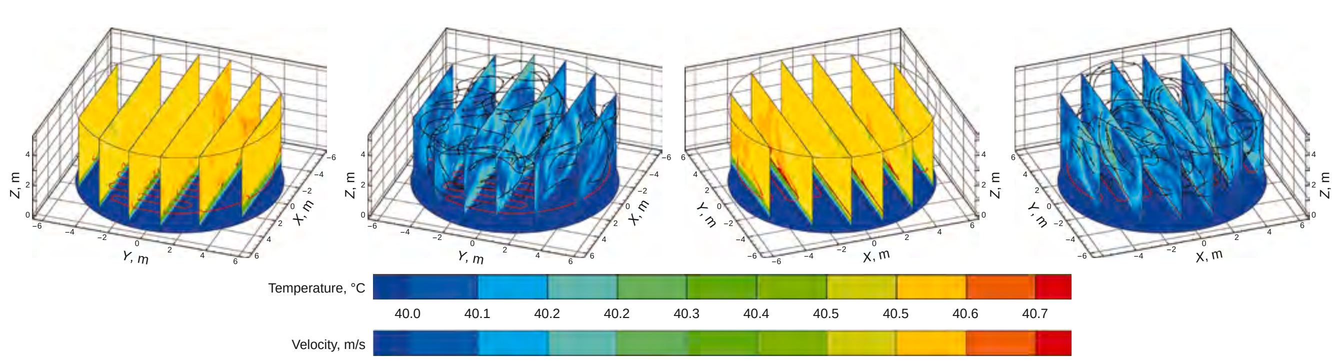

Fig. 36. 3D contour plots of physical fields in the computational domain (heated for 5 h).

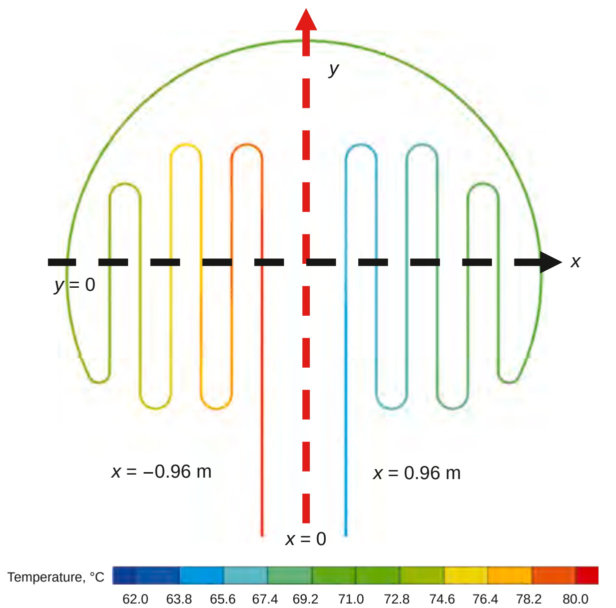

Fig. 37. Temperature distribution of water in the heating tube (heated for 5 h).

also be demonstrated by the simulation results shown in Fig. 36. Taking the $x = 0$ section as the center, the inlet of the heating tube is located in the $x < 0$ region. The heat transfer fluid first flows through this area, keeping the heating tubes in this region at a relatively high temperature, and the average oil temperature reaches 40.44 °C. The temperature variance in this area is relatively large (1.59 $°C^2$), because there are both high-temperature heating tubes and low-temperature crude oil at the bottom of the tank in this area, resulting in a significant temperature gradient. In the region where $x > 0$, since the temperature of the heat transfer fluid has decreased, the heating effect has weakened. The average oil temperature is 40.42 °C, and the temperature distribution is more uniform, with the variance reduced to 1.22 $°C^2$.

From the above data, it can be seen that although there are factors such as uneven distribution of heating tubes and cooling of the heat transfer fluid that lead to uneven heating of the crude oil within the computational domain, the three-dimensional convective flow field within the computational domain significantly reduces the non-uniformity of the temperature distribution. The velocity contour in Fig. 36 shows that in addition to the typical natural convection vortex structure centered around the heating tube, there are also a large number of complex flow structures such as lateral flow and inter-layer migration. These flows facilitate the transfer and diffusion of heat, effectively alleviating the temperature differences caused by uneven heating, making the average temperature differences among different areas insignificant, and the temperature variations only existing in local areas. The area with the lowest temperature is located near the bottom of the tank, beneath the heating tube. It is mainly caused by the natural convection effect where hot crude oil rises and cold crude oil sinks. Compared with existing studies, the overall three-dimensional physical field patterns in the storage tank during the tubular heating process remain consistent with earlier findings (Zhao et al., 2020, 2021, 2023a), which aligns with the established understanding in the field.

During the actual heating process of crude oil, a deep understanding of the heating pattern is the basis for optimizing the heating process and the operation of the storage tank. Therefore, the cross-section where the inlet and outlet of the heating tube are located (Figs. 38 and 39) was selected to analyze the evolution process of the temperature field when water is used as the heat transfer fluid, in order to explore the formation mechanism of the physical field shown in Fig. 36.

4.2.2. Analysis of the formation process of physical field

As shown in Figs. 38 and 39, during the 5-h heating process, the temperature fields on the two symmetrical sections evolved basically synchronously. After only 5 min of heating, a large area of the crude oil had begun to heat up, indicating that the heat provided by the heating tube rapidly spread throughout the entire computational domain through convection. As the heating process continues, the heat rises and spreads upwards from around the heating tube, this results in weaker heating of the crude oil located beneath the external surface of the heating tube, and the temperature difference between this area and other regions gradually increased. After heating for 1 h, the contour showed that a distinct low-temperature area appeared under the heating tube, At the same time, the upper boundary and the lateral boundaries also form a relatively thin layer of low temperature due to continuous heat dissipation and the fact that natural convection fails to fully cover them. As the heating time continues to increase, the temperature of the crude oil around and above the heating tube keeps rising, and the temperature difference between this crude oil and the bottom crude oil becomes even greater. Finally, a stable low-temperature zone approximately 0.3 m thick was formed at the bottom of the tank, while the thickness of the low-temperature zones at the

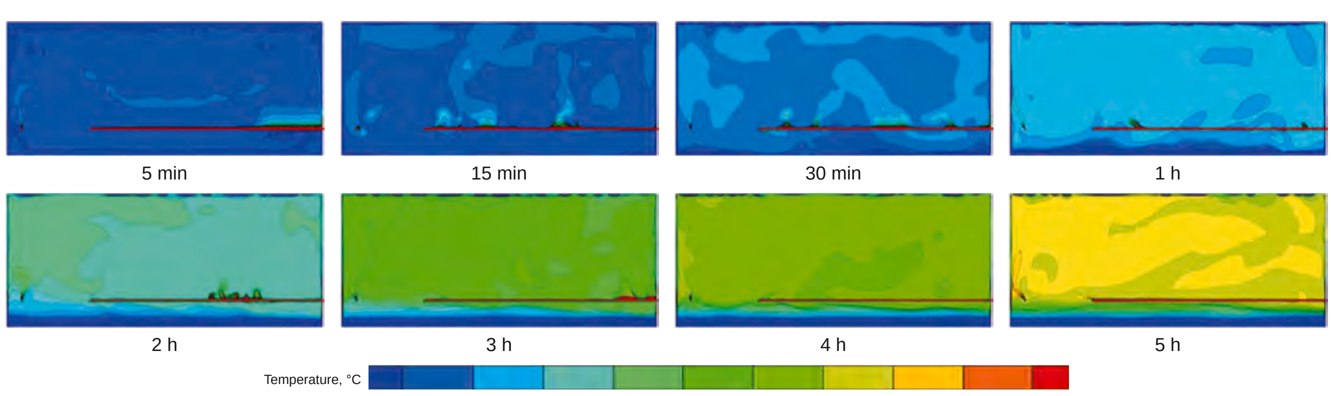

Fig. 38. Evolution process of the temperature field in the inlet section of heating tube ($x = -0.96$ m).

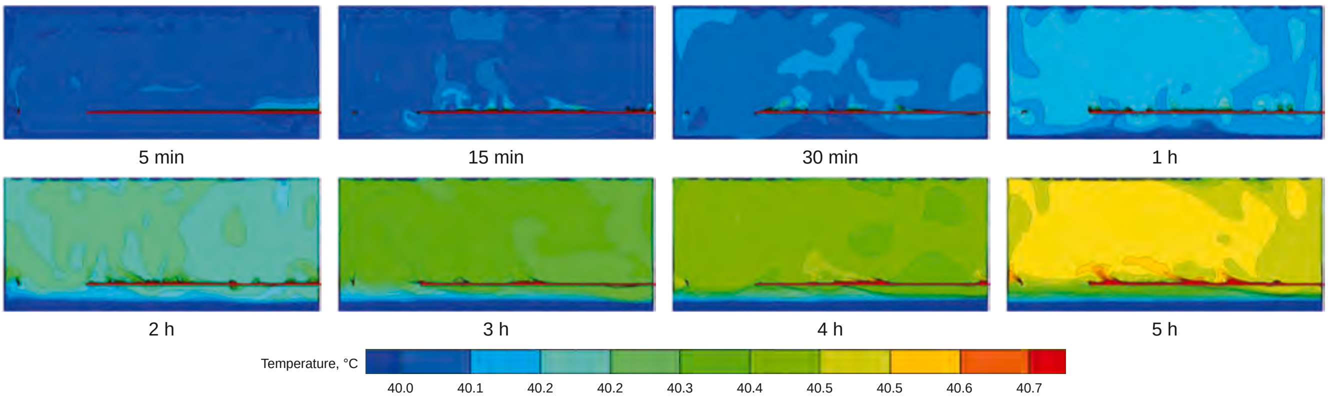

Fig. 39. Evolution process of the temperature field in the outlet section of heating tube (x = 0.96 m).

upper boundary and the side boundaries was 0.05 m and 0.09 m respectively. Despite a temperature difference exceeding 10 °C between the heating tubes themselves, the average oil temperature in the two corresponding sections differed by only 0.1 °C. This indicates that the lateral convection and inter-layer mixing effects within the computational domain are significant, effectively promoting the uniform distribution of heat. The temperature drop of the heat transfer fluid along the process did not have a significant impact on the overall temperature field. The formation of the low-temperature zone was mainly attributed to the fundamental characteristics of natural convective heat transfer.

4.3. Simulation results using nanofluid as the heat transfer fluid

4.3.1. Simulation results of three-dimensional physical field

Fig. 40 shows the three-dimensional temperature and velocity field contour of the calculation domain (the simulated storage tank) obtained through numerical simulation after heating for 5 h, using CuO-water nanofluid and graphene-water nanofluid as the heat transfer fluid. As shown in the figure, when using nanofluid as the heat transfer fluid, the temperature of the crude oil in the calculation domain increased more significantly after 5 h of heating. When using CuO and graphene-water nanofluid for heating, the average oil temperature increased from 40 to 40.51 and 40.46 °C respectively, and the average heating rate increased by 16% and 4.54%. Compared with the simulation results using water as the heat transfer fluid, when using nanofluid, the average temperature of the crude oil can be further increased. However, the temperature variance within the calculation domain has increased. The overall temperature variance within the calculation domain has increased from 1.41 $°C^2$ when water was used as the heat transfer fluid to 1.58, 1.45 $°C^2$ (as shown in Fig. 41(b)). Compared with the experimental results of the aforementioned small-scale models, the temperature rise rate of the actual oil storage tank is much lower. After being heated with CuO-water nanofluid for 5 h, the average temperature only increased by

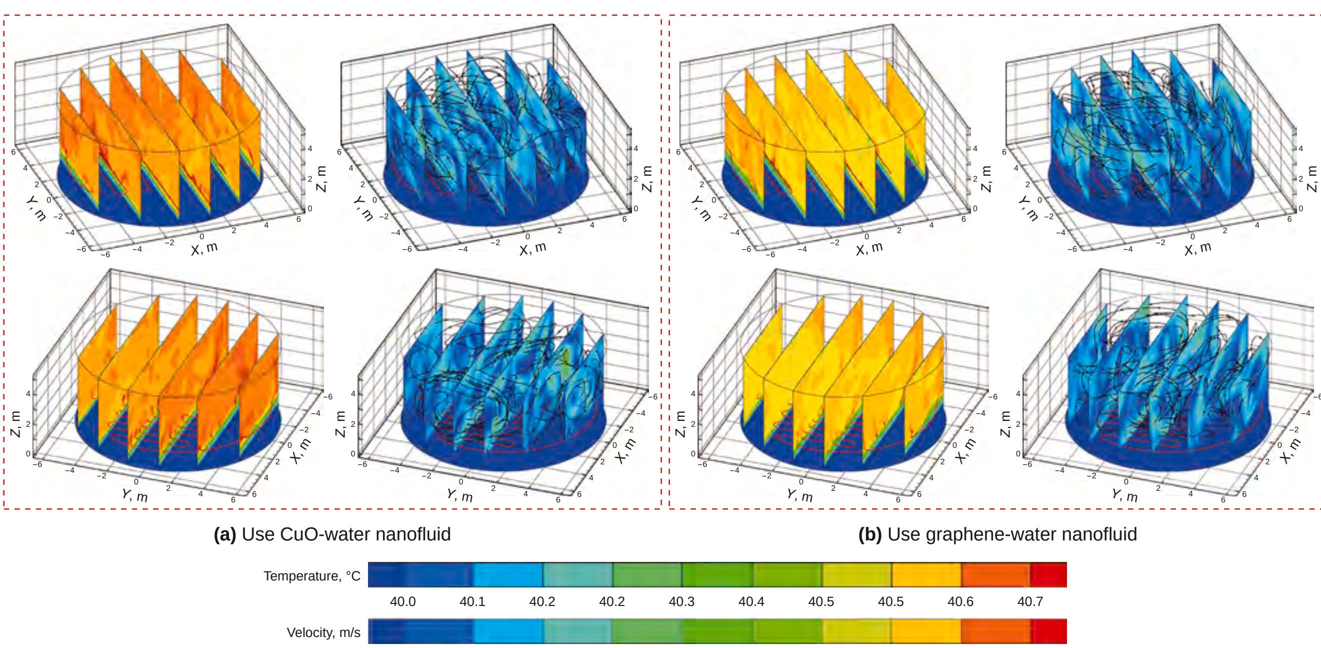

Fig. 40. 3D contour plots of physical fields in the computational domain (heated for 5 h with nanofluid).

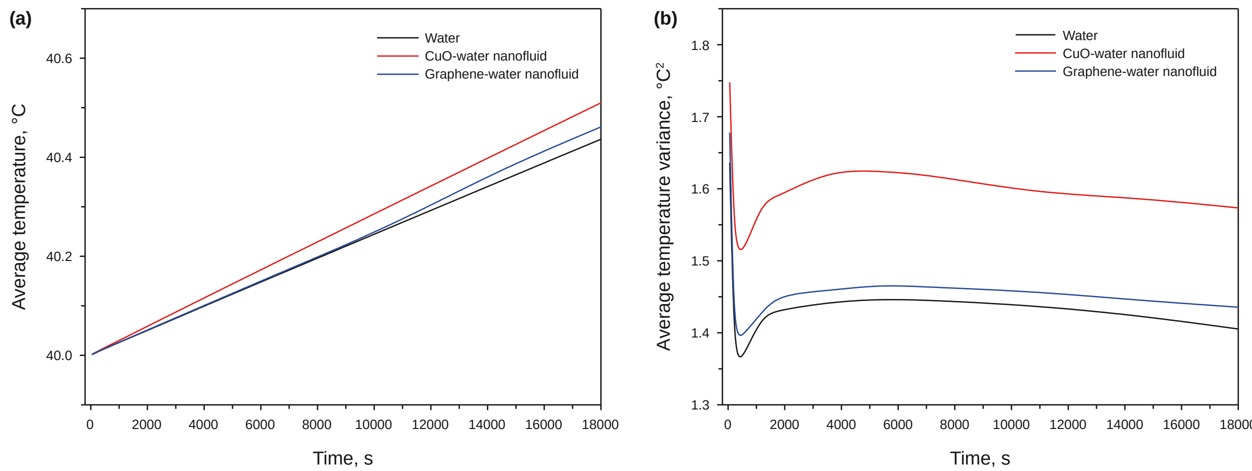

Fig. 41. Temperature characterization under different heat transfer fluids. **(a)** Average temperature; **(b)** Average temperature variance.

0.51 °C. The reason for this is that the actual oil storage tank has a much larger volume than the indoor experimental device, and its heat capacity is large, which significantly reduces the enhanced heat transfer effect of the nanofluid. Furthermore, the initial temperature of the indoor experiment (25 °C) was lower than the wax crystallization point of the crude oil. During the heating process, the latent heat effect of phase change was significant, and the nanofluid played a prominent role in breaking the wax crystal network and accelerating the wax dissolution. However, the actual initial temperature of the oil storage tank was set at 40 °C, which was higher than the wax crystallization point. During the heating process, single-phase convective heat transfer was dominant, and the enhanced advantages of the nanofluid in the phase change stage were not fully exerted.

As shown in Fig. 41(a), when nanofluid is used as the heat transfer fluid, the average temperature and the heating rate within the calculation domain have significantly increased, and they grow linearly over time. Although the increase in the average temperature is limited, it still brings considerable energy-saving benefits in large storage tank. From the temperature variance curve in Fig. 41(b), it can be seen that although the nanofluid can increase the average temperature within the computational domain, the temperature variance will also increase accordingly. This indicates that the degree of dispersion of the overall temperature distribution has increased, but it does not change the basic distribution law and macroscopic uniformity characteristics of the temperature field. The increase in variance is mainly due to the fact that the nanofluid enhances the local heat transfer near the tube wall, causing a significant increase in the temperature of the crude oil in that area. While in the regions far from the heating tube (such as near the bottom of the tank), the temperature rise is relatively small, resulting in an expansion of the local temperature difference. For example, the difference in temperature between the lower cold zone and the central oil temperature increased from 0.4 to 0.5 °C. Existing study, such as Lei et al. (2024), has found that mechanical stirring can achieve a more uniform temperature distribution within storage tanks. Similarly, the application of nanofluids in our work slightly reduces the extent of low-temperature zones by more effectively delivering heat to these originally cooler areas. This mechanism mitigates the risk of crude oil solidification at the tank bottom by elevating the overall temperature uniformity. From the perspective of the corresponding velocity field, after the use of nanofluid, significant three-dimensional flow characteristics still exist within the computational domain, but the overall speed values do not differ much. The stability of the velocity field distribution characteristics (including the overall level, positions of high and low speed zones) further indicates that the nanofluid have not caused any observable impact on the flow structure of the crude oil, neither bringing additional flow resistance nor causing instability in the flow pattern. Furthermore, compared to existing parameter optimization studies (Wang, 2018; Wu, 2022; Lei et al., 2024), our method enhances the tubular heating process simply by replacing the conventional heat transfer fluid with a nanofluid, without requiring any structural modifications to the storage tank or heating tubes.

4.3.2. Analysis of the formation process of physical field

Fig. 42 shows the temperature variations of three heat transfer fluid during their flow along the heating tube (points A to J). The nanofluid continues to dissipate heat to the crude oil during its flow, and the temperature gradually decreases. The outlet temperatures (point J) of the CuO and graphene-water nanofluid are 68.6 and 65.5 °C respectively, and the average temperature reduction rates are 0.13 °C/m and 0.159 °C/m respectively, which are significantly lower than that of water. The lower temperature drop of the CuO-water nanofluid can be attributed to two factors: Firstly, its thermal conductivity is approximately 1.36 times that of water, thereby enhancing the heat transfer efficiency per unit time; Secondly, its density is approximately 1.59 times that of water, resulting in a higher mass flow rate and heat capacity at the same flow rate. Although the specific heat capacity is slightly lower than that of water (about 91.8%), the overall heat capacity is still much higher than that of water. Therefore, the nanofluid not only enhances the heat transfer efficiency through its high thermal conductivity, but also maintains a relatively low temperature drop, thereby maintaining a higher average temperature along the heating tube. Together, this leads to an increase in the average temperature of the tube wall, increasing the effective heat transfer temperature difference between the wall and crude oil. The increased temperature difference is the key to facilitating more heat transfer to the crude oil, ultimately raising the average temperature of the crude oil in the tank.

Figs. 43 and 44 illustrate the evolution of the temperature fields of two typical sections of crude oil when CuO-water nanofluid is used as the heat transfer fluid. The results show that, consistent with the conclusions of the previous three-dimensional temperature field analysis, the evolution process of the temperature field and the distribution of high and low temperature zones are still mainly determined by the tank structure, the layout of the heating tube, and the physical and flow properties of the crude oil. Changing the heat

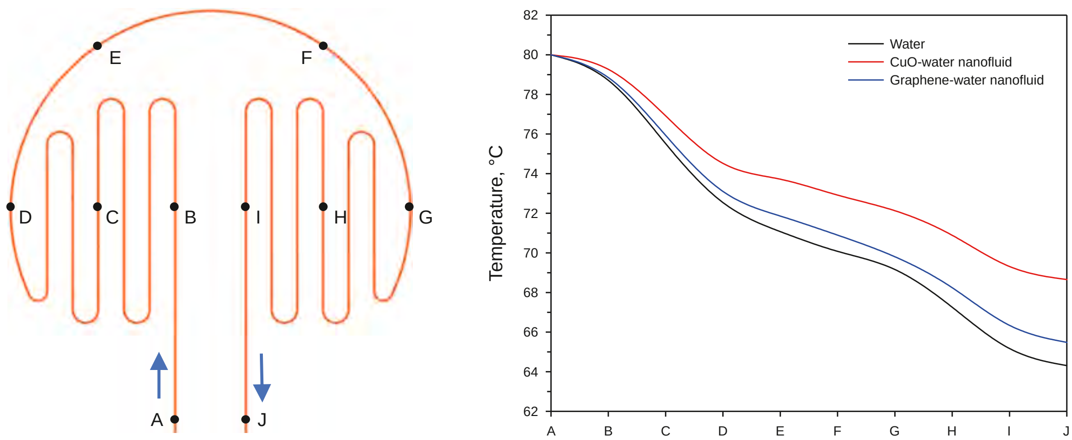

Fig. 42. Temperature distribution along heating tubes with different heat transfer fluids.

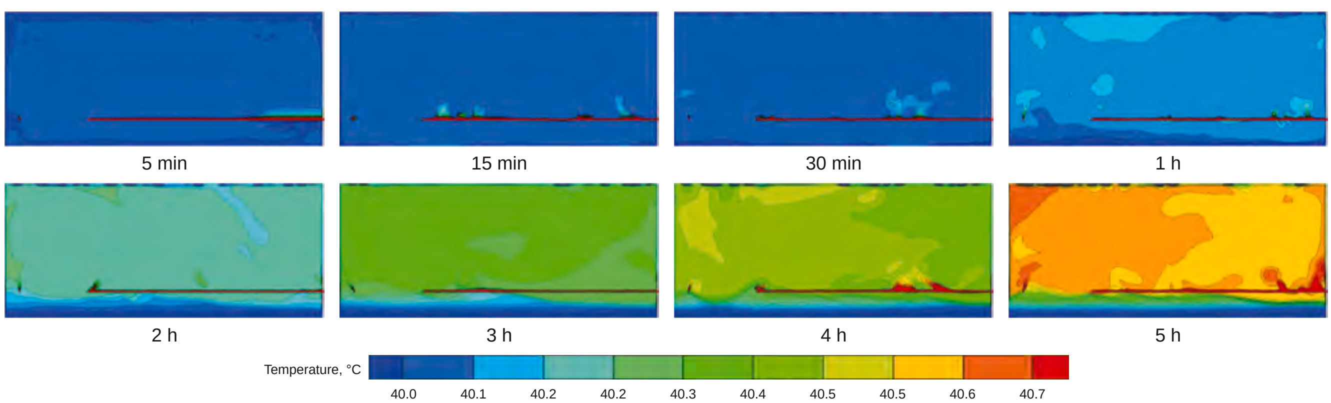

Fig. 43. Evolution process of the temperature field in the inlet section of heating tube ($x = -0.96$ m).

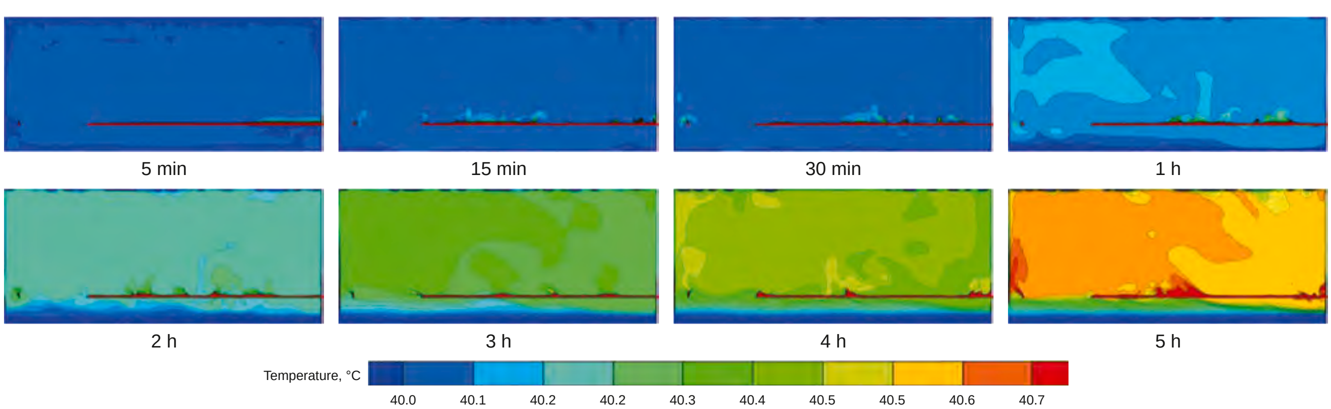

Fig. 44. Evolution process of the temperature field in the outlet section of heating tube ($x = 0.96$ m).

transfer fluid mainly affects the heat transfer rate and the final temperature level. However, due to the stronger heat transfer performance of nanofluid, the oil temperature in the typical profile is higher and the heating effect is better. At the same time, the temperature drop of the nanofluid along the heating tube is small, which results in a smaller temperature gradient along the length of the tube, and the difference in the average temperature of the outer wall of the heating tube at different profiles is also reduced accordingly, which helps to promote the uniformity of the temperature field within the computational domain. The contours show that in the area where the heating tube is more densely distributed, the oil temperature is higher, but the difference is not significant. The low-temperature zone still remains close to the bottom of the tank, and its existence is limited by the relatively low thermal conductivity of the crude oil and the intensity of natural convection.

Still, the temperature of <40.2 °C is defined as low-temperature crude oil. Fig. 45 shows the change in volume over time under different heat transfer fluid. In the initial heating stage, the volume of the low-temperature crude oil decreased rapidly, dropping from 233.6 to 48.2 m^3 within 0.15 h, and the reduction effect was

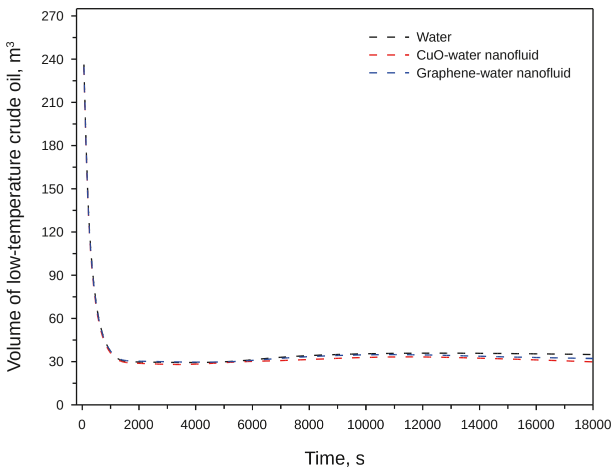

Fig. 45. Volume of low-temperature crude oil in the computational domain.

independent of the heat transfer fluid. After 0.3 h of heating, approximately 30.3 m^3 of low-temperature crude oil that was difficult to continue heating remained in all types of heat transfer fluid. This volume was relatively stable and was not affected by the heat transfer fluid. The results indicate that this portion of the residual low-temperature crude oil is an inherent “low-temperature zone” determined by the tank structure and the properties of the crude oil. Enhancing the performance of the heat transfer fluid cannot effectively eliminate this.

4.3.3. Analysis of heat transfer mechanism

The average convective heat transfer coefficient between the heating tube inner wall and the outer wall, as well as the total heat dissipation of the computational domain, are presented in Fig. 46. Nanofluid, with their higher thermal conductivity and moderate specific heat capacity, synergistically enhance the convective heat transfer within the tube and slow down their own temperature drop, thereby improving the heating effect on crude oil. During the tubular heating process, the nanofluid enhances the forced convective heat transfer within the tube by increasing the *Pr* number. The convective heat transfer coefficients within the tube for CuO and graphene-water nanofluid correspondingly reach 56.91 and 54.47 W/(m^2·K). The enhancement of internal heat exchange has increased the temperature of the tube wall and enlarged the heat transfer temperature difference (ΔT) with the crude oil. Although the heat transfer coefficient on the crude oil side remains basically unchanged, according to $Q = h{\cdot}A{\cdot}\Delta T$, the increase in ΔT significantly increases the heat dissipation. The convective heat transfer coefficient outside the tube also increases from 52.85 W/(m^2·K) of the water to 56.31 and 53.93 W/(m^2·K). The increase in the heat transfer coefficients of the inner and outer tube walls is approximately 9%. Although the physical properties of different nanofluid vary, their thermal conductivity and thermal diffusion performance are all superior to water. Therefore, during stable heating, the convective heat transfer coefficients inside and outside the tube can be simultaneously enhanced, and the enhancement amplitude varies depending on the properties.

When water is used as the heat transfer fluid, the heat loss after 5 h of heating is 16,059 W. After switching to nanofluid, due to their stronger thermal diffusion ability, the overall temperature rises, and the temperature difference between the inside and outside of the tank increases. Based on the degree of increase in the average temperature, the heat loss also increases slightly. When using CuO-water nanofluid, the overall heat loss is the

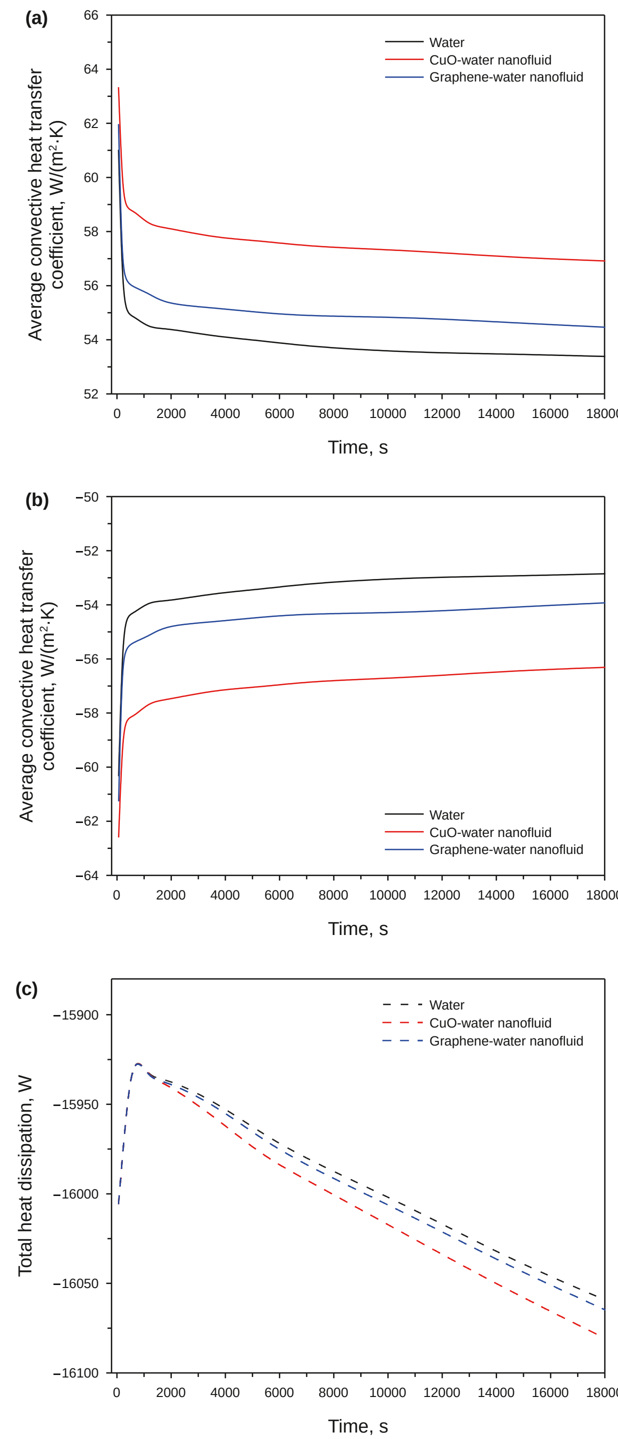

Fig. 46. Heat transfer characteristics of the system. **(a)** Average inner-wall convective HTC; **(b)** Average outer-wall convective HTC; **(c)** Total heat dissipation.

largest, at 16,080 W, which is only an increase of 0.18% compared to when water is used as the heat transfer fluid.

Fig. 47(a) illustrates the distribution of the thermal boundary layer on the inner wall of the heating tube under different heat transfer fluid. When using nanofluid (especially CuO-water nanofluid), the thermal boundary layer on the inner wall becomes significantly thinner. According to the theory of forced convection, the thickness of the thermal boundary layer $\delta_{\mathrm{t,in}} \propto \mu/k{\cdot}Re^{-0.5}$. The high thermal conductivity of the nanofluid promotes the radial

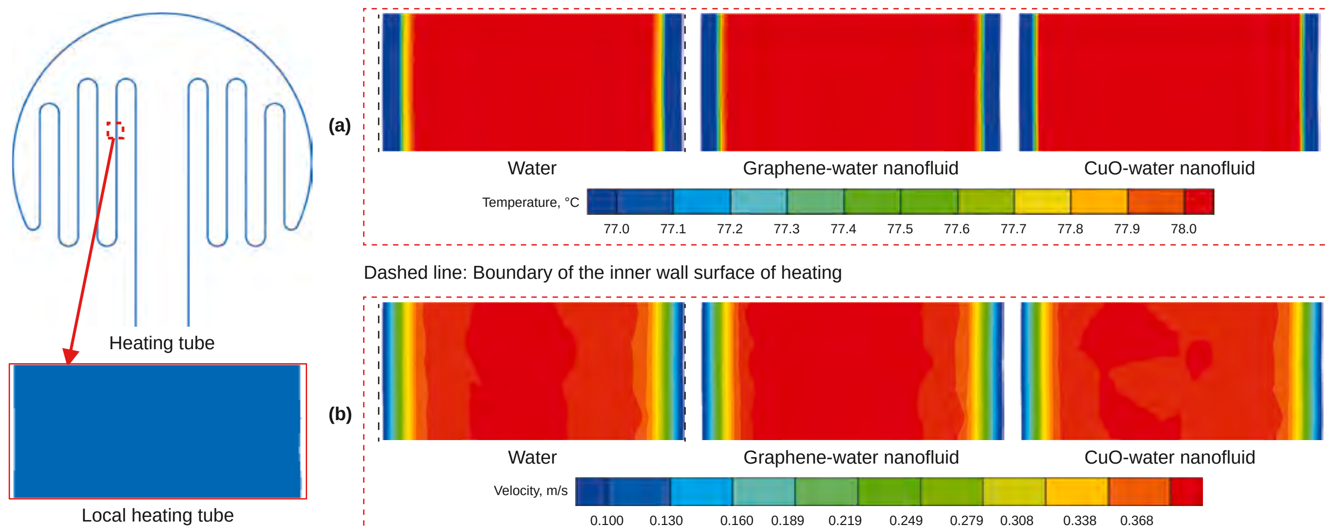

Fig. 47. Local contour plot of boundary layer at inner wall of heating tube.

diffusion of heat from the tube wall to the fluid, inhibits the accumulation of heat in the near-wall region, and thus reduces the thickness of the thermal boundary layer. When water is used as theheat transfer fluid, the thickness of the thermal boundary layer is 3.2 mm. When CuO and graphene-water nanofluid are used, it decreases to 2.4 and 2.7 mm respectively, which is 25% and 15.6% less than that of water. Fig. 47(b) shows the velocity boundary layer contour for the corresponding heat transfer fluid. The thicknesses of the velocity boundary layers for water, CuO and graphene-water nanofluid are 1.7, 1.5, and 1.3 mm. According to Newton's law of viscosity, the thickness of the velocity boundary layer $\delta_{\mathrm{v,in}} \propto \mu/\rho u$. After using nanofluid, the wall temperature gradient increases, the local viscosity decreases, the velocity gradient increases, and at the same time, parameters such as density and buoyancy force also change. All these factors jointly lead to a change in the flow state and a thinning of the velocity boundary layer, thereby strengthening the forced convection within the tube. This result is consistent with the patterns shown in Fig. 46(a) and (b).

Fig. 48 shows the changes in the thermal boundary layer and velocity boundary layer on the outer wall of the heating tube. Observing the figure, it can be seen that, contrary to the inner wall, the nanofluid causes the thermal boundary layer and velocity boundary layer on the outer wall of the heating tube to simultaneously thicken. On the one hand, the morphology of the outer wall thermal boundary layer is controlled by the tube wall temperature and the physical properties of the crude oil. Due to the high convective heat transfer coefficient within the tube (as shown in Fig. 46(b)), the tube wall maintains a higher temperature. For natural convection, the effective thermal resistance can be characterized by the boundary layer thickness, which is expressed as:

$$\delta_{\mathrm{th,out}} = \int_0^{\infty} \left(1 - \frac{T - T_\infty}{T_\mathrm{w} - T_\infty}\right) \mathrm{d}y \tag{29}$$

As the tube wall temperature T_w increases, the effective thermal resistance thickness also becomes larger. Although the geometric thickness increases, due to the deep penetration of heat into the crude oil domain (as shown in Fig. 48(a), the red high-temperature area expands), the actual thermal resistance actually decreases. On the other hand, due to the higher thermal conductivity of nanofluid, heat can be transferred more efficiently

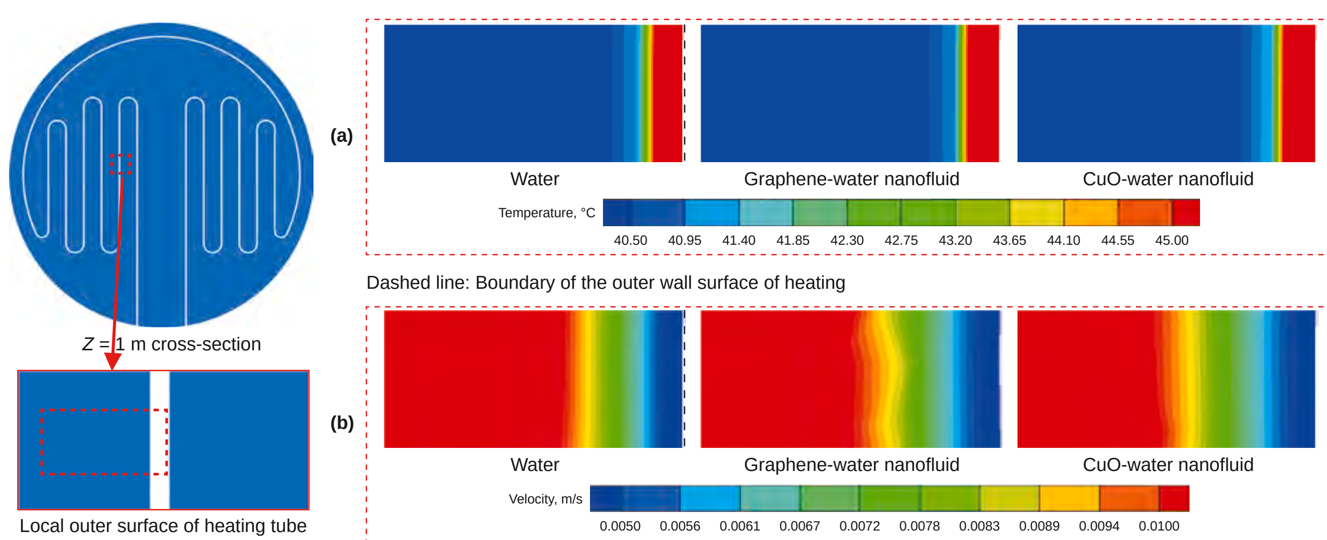

Fig. 48. Local contour plot of boundary layer at outer wall of heating tube.

from the outer wall of the heating tube to the crude oil inside the tube. In the area near the outer wall, the range of heat diffusion significantly expands, the thermal boundary layer gradient increases, and the thickness of the boundary layer becomes thicker accordingly. Especially when using CuO-water nanofluid, the thickness of the boundary layer increases from 2.4 mm when using water to 2.8 mm. At the same time, it can be clearly observed that the velocity boundary layer becomes thicker (the yellow to blue area in Fig. 48(b)), the temperature difference between the outer wall of the heating tube and the temperature of the crude oil increases, which enhances the buoyancy force of the crude oil near the outer wall, strengthening the natural convection effect, resulting in an increase in the flow velocity of the crude oil near the boundary layer and an increase in the velocity gradient, and consequently, the velocity boundary layer also becomes thicker.

The initial temperature for the actual size tank simulation was set at 40 °C, which is above the gel point of the crude oil, based on practical engineering considerations: during normal operation, the temperature of crude oil in storage tanks is typically maintained above the gel point to ensure flow safety. This choice results in a difference in the physical processes under investigation compared to the small-scale experiment. The small-scale experiment (initial temperature of 25 °C) simulates a cold-start process from a fully gelled state, where the core issue is gel melting accompanied by significant latent heat of phase change. The heat input is primarily used to disrupt the wax crystal structure, and the advantage of nanofluids lies in their ability to deliver the melting latent heat more rapidly, thereby accelerating the phase transition process. In contrast, the actual size simulation (initial temperature of 40 °C) represents a daily thermal maintenance scenario, where the crude oil remains in a single-phase liquid state, and heat transfer is dominated by buoyancy-driven single-phase natural convection. Under these conditions, the higher thermal conductivity of nanofluids directly enhances heat transfer efficiency and further intensifies natural convection. Simulation results demonstrate that, even in the single-phase regime, nanofluids achieve higher heating rates and improved temperature uniformity compared to water by thinning the thermal boundary layer and enhancing convective intensity. This confirms that the advantages of nanofluids are not limited to accidental cold-start situations but are also applicable to a broader range of daily engineering scenarios.

4.4. Analysis of the effect of heating tube layout optimization

To evaluate the synergistic enhancement effects of heating tube layout optimization and nanofluids on tube-based heating, this study designed two simulation cases with a densified coil layout: Case 4 (densified layout + water) and Case 5 (densified layout + CuO-water nanofluid). As shown in Fig. 49 (evolution of the temperature field in the inlet section of the heating tube), compared with the conventional layout, the high-temperature zone coverage is significantly expanded during the middle and later heating stages (3 h, 5 h) under the densified layout (Case 4). After 5 h of heating, the low-temperature zone near the tank bottom is reduced from the original 0.3 to 0.12 m, and the domain-average temperature increases by 0.11 °C compared to the conventional layout (Case 1) (Fig. 50(a)).

When CuO-water nanofluid is further applied as the heat transfer fluid based on the densified layout (Case 5), the enhanced heat transfer inside the tubes due to the high thermal conductivity of the nanofluid, combined with the larger heat exchange area provided by the densified layout, results in the highest temperature level throughout the heating process for Case 5, as shown in Figs. 49 and 50(a). The local temperature in the inlet section of the heating tube reaches up to 40.75 °C, and the domain-average temperature after 5 h of heating is further raised to 40.66 °C. Moreover, the corresponding volume of low-temperature crude oil for Case 5 is only 23.3 m^3, which is 31% lower than that of the conventional layout (Fig. 50(b)).

In summary, the densified layout strengthens the heat diffusion into the deeper crude oil by increasing the heating area and reducing heating blind spots. When combined with active heat transfer enhancement techniques such as nanofluid, a significant synergistic effect can be achieved, which not only improves the overall temperature level of the storage tank but also more effectively reduces the inherent "low-temperature zone", providing a feasible optimization approach for achieving efficient and uniform heating in large storage tanks.

4.5. Energy consumption analysis

Taking the average temperature, average temperature variance and heating efficiency at $t = 5$ h as evaluation indicators, as shown in Table 5, heating efficiency: energy obtained by heating crude oil/the heat provided by the heating tube.

As shown in Table 5, under the same heating conditions, changing the different heat transfer fluid will affect the overall average temperature, heating efficiency and temperature uniformity. Although the average temperature variance increases when using nanofluid, nanofluid has positive effects on tubular heating. Among them, the CuO-water nanofluid has a more significant effect. The heating efficiency is increased by 3.88%, and the average heating rate is increased by 16%. However, it still needs to be judged as the optimal heat transfer fluid based on multiple

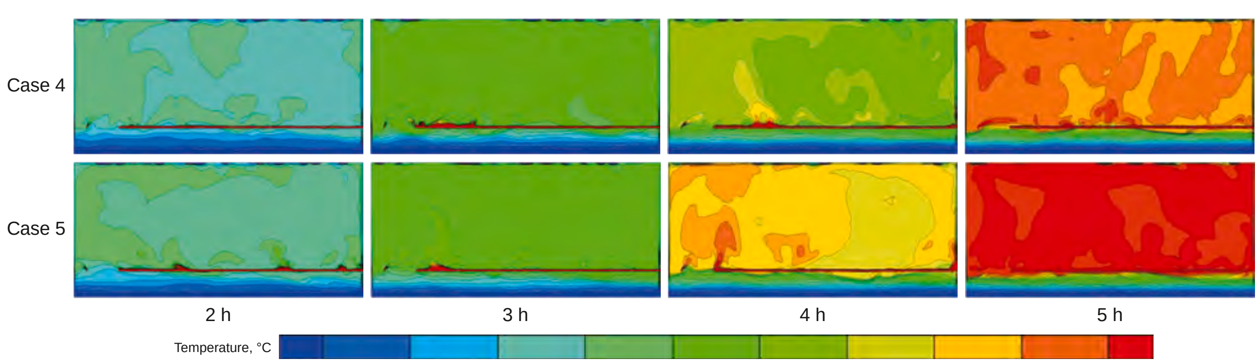

Fig. 49. Evolution process of the temperature field in the inlet section of heating tube ($x = -0.4$ m).

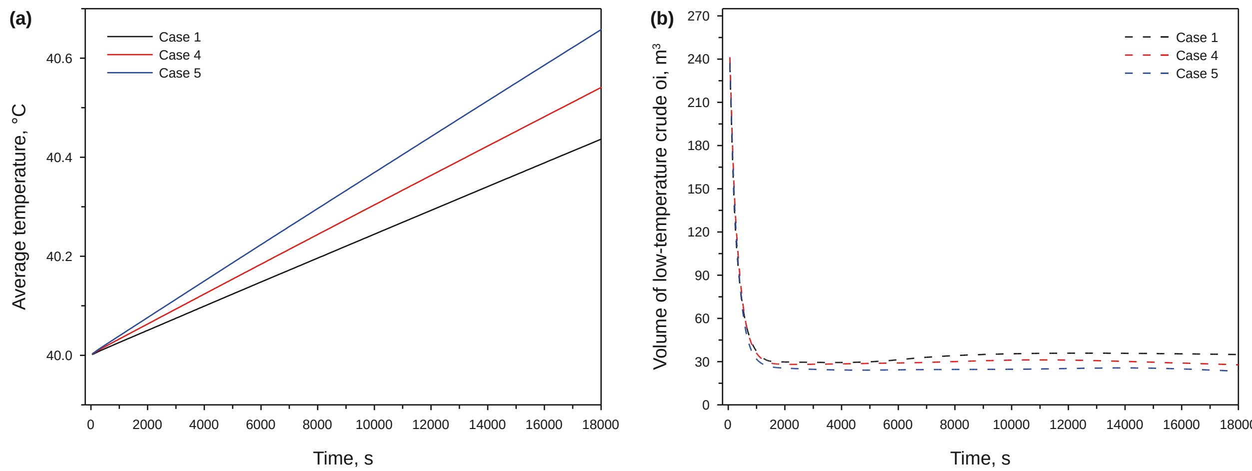

Fig. 50. Temperature characterization under different heating tube layouts. **(a)** Average temperature; **(b)** Volume of low-temperature crude oil.

Table 5
Evaluation indicators for different heat transfer fluids.

Heat transfer fluid	Average temperature, °C	Average temperature variance, $°C^2$	Heating efficiency
Water	40.44	1.4	71.05%
Graphene-water nanofluid	40.46	1.45	72.37%
CuO-water nanofluid	40.51	1.58	74.93%

Table 6
Energy consumption required by different heat transfer fluids.

Heat transfer fluid	Energy consumption for heating for 5 h, J	Energy consumption during the operation of the pump for 5 h, J	Total energy consumption, J
Water	407,375,080	34,700,000	442,075,080
Graphene-water nanofluid	399,546,770	38,020,000	437,566,770
CuO-water nanofluid	386,280,520	41,920,000	428,200,520
Water (inlet temperature +5 °C)	466,197,000	34,700,000	500,897,000
Graphene-water nanofluid (inlet temperature +5 °C)	456,241,910	38,020,000	494,261,910
CuO-water nanofluid (inlet temperature +5 °C)	442,725,140	41,920,000	485,745,140
Graphene-water nanofluid (halved concentration)	402,520,810	36,080,000	438,600,810
CuO-water nanofluid (halved concentration)	394,652,900	40,120,000	434,772,900

Table 7
Gas consumption and carbon emissions by different heat transfer fluids.

Heat transfer fluid	Annual required amount of natural gas, m^3	Price of natural gas, yuan	Carbon emissions, ton
Water	22,432	66,623	48.50
Graphene-water nanofluid	22,006	65,357	47.58
CuO-water nanofluid	21,278	63,196	46.01
Water (inlet temperature +5 °C)	25,676	76,258	55.52
Graphene-water nanofluid (inlet temperature +5 °C)	25,126	74,624	54.33
CuO-water nanofluid (inlet temperature +5 °C)	24,386	72,426	52.73
Graphene-water nanofluid (halved concentration)	22,172	65,851	47.94
CuO-water nanofluid (halved concentration)	21,736	64,556	47.00

indicators. In addition, different conditions should be considered, including energy consumption, natural gas usage, and carbon emissions, as shown in Tables 6 and 7.

The power for the internal circulation of the heating tube is provided by the pump. Based on actual field conditions in oilfields and considering a pump efficiency of 80%, its operating energy consumption is calculated as follows:

$$E = \frac{\Delta p \cdot Q}{\eta} \times t \tag{30}$$

The energy consumption for circulating water as the heat transfer fluid over 5 h was calculated to be 34,700,000 J. However, nanofluids, due to their higher viscosity and density, increase the system pressure drop, thereby resulting in higher energy consumption. The relationship between nanofluid concentration and viscosity, pumping power, and net efficiency is illustrated in Fig. 51. As shown in the figure, although the CuO-water nanofluid requires more pump power compared to the graphene-water nanofluid, its overall efficiency has increased by 2.44% due to its superior heat transfer performance.

According to the principle of energy conservation, the energy provided by the heating furnace should equal the sum of the energy absorbed by the heated crude oil and the total heat

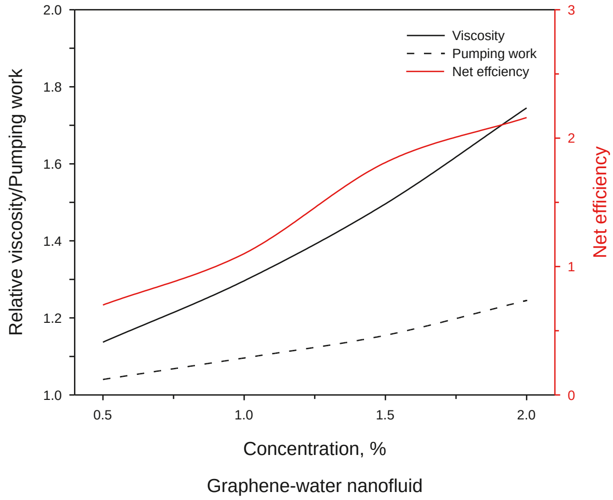

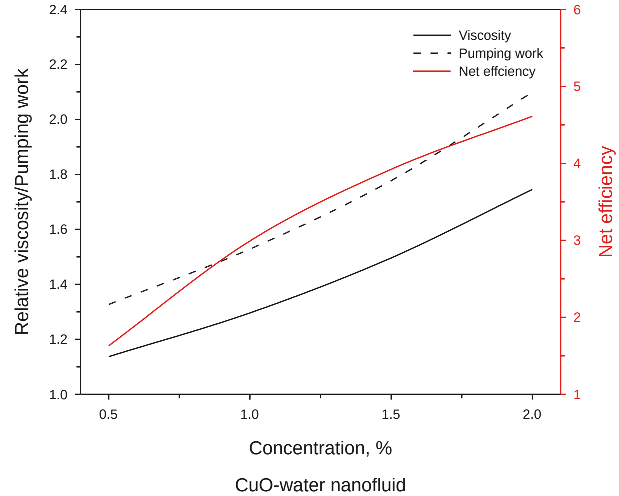

Fig. 51. Relationship between nanofluid concentration and viscosity, pumping work, and net efficiency.

dissipation loss of the tank system. This total energy can be approximately regarded as equivalent to the heat released by the heat transfer fluid during the circulation process. Therefore, the effective output heat of the heating furnace can be indirectly obtained by calculating the latter, while considering the energy transfer efficiency of the heating furnace to be 85%. The total energy consumption of heating furnace = Effective output heat/Heating furnace efficiency. The energy consumption corresponding to different heat transfer fluids after 5 h of heating is thus obtained. As shown in Table 6, when using CuO-water nanofluid as the heat transfer fluid, the total energy consumption is 428,200,520 J, which represents a reduction of 3.1% compared to the energy consumption when using water.

The price of natural gas is 2.76 yuan/m^3, its main is CH_4, which releases a significant amount of thermal energy during combustion. According to Chinese standards, the lower heating value of natural gas is approximately 35.588 MJ/m^3. Therefore, 1 m^3 of natural gas is equivalent to 35,588,000 J. Using this heating value for energy conversion, the annual natural gas consumption is calculated as:

$$V_{gas} = \frac{E_{total}}{\eta \times Q_{gas}} \tag{31}$$

The internationally established emission factor for natural gas is typically 2.1622 kg/m^3. Thus, the carbon emissions (in tonnes) are calculated as: Carbon emissions (t) = natural gas consumption (m^3) × emission factor (kg/m^3)/1000. As summarized in Table 7, using CuO-water nanofluid as the heat transfer fluid reduces natural gas consumption by 5.14% and carbon emissions by 4.9% compared to using water. When the concentration of the nanofluid is halved, the total energy consumption of the system decreases by 1.2% and 3.1% for graphene-water nanofluid and CuO-water nanofluid, respectively, compared to water. Correspondingly, carbon emissions are reduced by 1.1% and 3%. When the heating tube temperature is raised to 85 °C, the total energy consumption, natural gas usage, and carbon emissions increase for all heat transfer fluids, yet the nanofluids still demonstrate better performance across all metrics.

The economic analysis based on the total investment is shown in Table 8. Graphene-water nanofluid is economically unfeasible due to its prohibitively high cost. In contrast, CuO-water nanofluid demonstrates exceptional economic performance, with an initial investment of only 20,320 yuan. Owing to its outstanding energy-saving effect, this investment can be fully recovered through savings in gas costs in as little as 1.2 years. From the perspective of the total five-year operational cost, using CuO-water nanofluid only increase overall expenses by 1.1% compared to using water as the heat transfer fluid.

Based on extensive existing research and the experimental results of this work, across-sectional comparison was conducted between the CuO-water and graphene-water nanofluids focused on in this study and the commonly reported Al_2O_3-water nanofluid and Al_2O_3-SiO_2-water hybrid nanofluid. The comparison criteria mainly include: (i) heat transfer performance, (ii) economic cost, and (iii) stability and practicality (comprehensively considering stability, viscosity increase, and energy consumption reduction). Based on the above criteria, the performance comparison of the nanofluids is shown in Table 9.

Although graphene possesses top-tier thermal conductivity, its high cost severely restricts its large-scale engineering application. The Al_2O_3-water nanofluid, with its low cost and good stability, is a widely studied medium, but its thermal conductivity enhancement is significantly lower than that of CuO-water nanofluid. The

Table 8
Comprehensive economic analysis.

Cost item	Water	Graphene-water nanofluid	CuO-water nanofluid
Cost of nanoparticles, yuan	0	3,762,000	20,320
5-year natural gas cost, yuan	333,115	326,785	315,980
5-year operating cost, yuan	333,115	4,088,785	336,300
Cost changes	Criterion	+12.27%	+1.1%
Investment payback period, years		>100	1.2

Table 9
Benchmarking of alternative nanofluid and hybrid materials.

Materials	Heat transfer performance (weighting 40%)	Economy (weight 35%)	Stability and practicality (weight 25%)	Synthesis score
Graphene-water nanofluid	4	1	3	2.7
CuO-water nanofluid	5	4	4	4.4
Al_2O_3-water nanofluid	3	4	4	3.6
Al_2O_3-SiO_2-water nanofluid	4	5	2	4.1

emerging Al_2O_3-SiO_2-water nanofluid exhibits relatively good heat transfer performance and lower cost; however, its preparation process is complex and its stability is poor.

Considering all the above analyses, the CuO-water nanofluid demonstrates advantages in energy consumption, economic cost, heating efficiency, and environmental performance, making it the optimal heat transfer fluid.

5. Conclusions

(1) Laboratory experiments demonstrate that nanofluids exhibit effective heating enhancement for crude oils with different gel points and wax contents. CuO-water nanofluid significantly improves heating performance, accelerating temperature rise at both the bottom and top sections, shortening thermal lag time, reducing radial temperature differences, and promoting more uniform temperature distribution. Its heating rate exceeds that of graphene-water nanofluid and pure water, completing the heating process approximately 25% faster than water, thus exhibiting the best performance, followed by graphene-water nanofluid.

(2) Based on experimental data, a numerical model was developed that couples phase-change heat transfer with an unstructured mesh, incorporating non-Newtonian behavior and the mechanisms of coupled natural and forced convection. The simulations show good agreement with experimental results with low average relative error, successfully reproducing the evolution of gelled oil, temperature stratification, and convective structures. This model provides a reliable theoretical tool for the heating design of large oil storage tank.

(3) Both experiments and simulations indicate that nanofluid accelerate the transition of waxy crude oil from gel to sol state. CuO-water nanofluid achieves heating and induces the sol state in a shorter time. During the initial heating stage, a “thermal shell” forms, reducing thermal resistance; in the mid-phase, strong natural convection emerges, shifting heat transfer from radial conduction to global convection; in the later stage, convection promotes more uniform heat distribution. In contrast, the heating performance of pure water is less effective, resulting in a larger volume of crude oil remaining in the gelled state at the end of the process.

(4) Numerical simulations of actual size oil storage tank reveal that while nanofluid do not alter the macroscopic temperature field structure dominated by heater layout and natural convection, they significantly enhance heat transfer performance. Both CuO and graphene-water nanofluid increase the average temperature and improve heating efficiency, effectively transferring heat to originally low-temperature regions and enhancing overall temperature uniformity. They also strengthen convective heat transfer inside and outside the heating tubes, outperforming conventional heat transfer fluids in overall performance. Coupling a densified heating tube layout with nanofluids further increases the in-tank temperature while reducing the low-temperature zone.

(5) The enhanced heat transfer mechanism of nanofluid stems from their higher thermal conductivity and moderate specific heat capacity, which delay temperature drop along the flow path, significantly reduce the thermal boundary layer thickness inside the tube (by 25% for CuO-water nanofluid), and increase the effective temperature difference between the tube wall and the crude oil. Outside the tube, the thermal boundary layer thickens and thermal penetration depth increases, yet the actual thermal resistance decreases, accompanied by significantly enhanced natural convection. Coupled with simultaneous optimization of the velocity boundary layer, nanofluid achieve synergistic enhancement of forced convection inside the tube and natural convection outside.

(6) The core advantage of using nanofluids in crude oil storage tank heating lies in its ability to enhance the performance of the tubular heating system simply by replacing water with nanofluids, requiring no modifications to existing heating tubes or equipment. However, this study has several limitations. Firstly, the numerical simulations employed a homogeneous single-phase model, which does not fully account for micro-scale effects such as nanoparticle migration and aggregation. Secondly, the model incorporates certain scale-up simplifications and was only validated against the cooling process of an actual storage tank, lacking experimental data to support the heating process using nanofluids in storage tank. Finally, the assessment of the long-term stability and production costs of nanofluids remains insufficient.

(7) To achieve large-scale industrial application, several key challenges must be addressed. One is the potential aggregation and sedimentation of nanoparticles under prolonged circulation and heating, which could compromise their stability and heat transfer performance. Another is the need to evaluate the risk of clogging in pumps, valves, and pipelines caused by nanofluids. Additionally, constrained by natural convection, a low-temperature zone at the tank bottom persists. Future work could focus on developing more accurate multiphase flow models and enhancing agitation at the tank bottom through asymmetric tube arrangement, the installation of guide structures, or integration with mechanical stirring. These improvements would further optimize temperature uniformity and ultimately facilitate the industrial adoption of this technology.

CRediT authorship contribution statement

Jian Zhao: Writing – original draft. **Zhen-Dong Yang:** Writing – review & editing. **Fan Li:** Formal analysis. **Hang Dong:** Data curation. **Zhi-Hua Wang:** Investigation.

Declaration of competing interest

There is no conflict of interest.

Acknowledgements

This work is supported by the National Natural Science Foundation of China (Grant no. 52304065, Grant no. 52474078).

References

BP, 2023. BP Energy-Outlook 2023.
Chen, W.Z., Wang, S., Zhai, Y.L., et al., 2023. Effect of aggregation state on the thermal conductivity of nanofluids. Chem. Ind. Eng. Prog. 42 (11), 5700–5706 (in Chinese). https://doi.org/10.16085/j.issn.1000-6613.2022-2257.
Dong, H., Guo, N., Zhang, L.J., et al., 2023. Effect of tubular heater structures on the thermal behaviors of waxy crude oil. Case Stud. Therm. Eng. 47, 103078. https://doi.org/10.1016/j.csite.2023.103078.
Dong, H., Zhang, S.K., Zhao, J., et al., 2025. Heat transfer research on the cooling process of waxy crude oil storage in the vault tank based on VOF model. Appl. Therm. Eng. 258, 124657. https://doi.org/10.1016/j.applthermaleng.2024.124657.
Fang, Y.B., 2025. Research on Stability of Water-based Fe_3O_4/Cu Nanofluids and Heat Collection Characteristics Under Magnetic Field Enhancement. Qingdao

University of Technology. Master's thesis (in Chinese). https://doi.org/10.27263/d.cnki.gqudc.2025.001162.
Ge, F.M., 2024. Research on the development of China's petroleum and petrochemical industry in the context of low-carbon economy. Bohai Econ. Outlook (7), 67–70 (in Chinese). https://doi.org/10.16457/j.cnki.hbhjjlw.2024.07.012.
Gao, B.Y., Ge, H.J., Li, H.S., 2024. Research and application of segmented online electromagnetic heating wax removal system for oil pipeline. Petrochem. Ind. Autom. 60 (6), 86–88. https://doi.org/10.3969/j.issn.1007-7324.2024.06.020 (in Chinese).
Gao, B.Y., Ge, H.J., Li, H.S., et al., 2025. Research and application of intelligent electromagnetic heating wax removal system for oil wells. Petrochem. Ind. Autom. 61 (1), 22–24 (in Chinese). https://doi.org/10.3969/j.issn.1007-7324.2025.01.005.
Hu, Z.Y., Ma, B.S., Wang, G., 2024. Numerical study on natural convection of Cu-water nanofluid in a trapezoidal cavity under an inclined magnetic field. J. Gansu Sci. 6 (5), 83–89 (in Chinese). https://doi.org/10.16468/j.cnki.issn1004-0366.2024.05.012.
Li, M., Zou, Y., Zhang, X., et al., 2020. Research on heat transfer of nanofluids in built-in helical spring heat exchange tubes. Chem. Eng. Equip. (12), 215–217 (in Chinese). https://doi.org/10.19566/j.cnki.cn35-1285/tq.2020.12.091.
Lei, M.Y., Zhao, J., Wang, H.T., et al., 2024. Effect of mechanical stirring on heat transfer and flow of crude oil in storage tanks under different heating methods. Case Stud. Therm. Eng. 58, 104382. https://doi.org/10.1016/j.csite.2024.104382.
Li, H.C., 2023. Study on Enhanced Heat Transfer and Stability Characteristics of Al_2O_3-SiO_2/Water Hybrid Nanofluids. Wuhan University. Master's thesis (in Chinese). https://doi.org/10.27379/d.cnki.gwhdu.2023.000698.
Ma, K.R., Zhang, Q.W., Li, S.Q., et al., 2020. Numerical simulation study on the heating process of thermal oil in crude oil storage tanks based on CFD. J. Hebei Univ. Water Resour. Electr. Power 30 (3), 32–36+47 (in Chinese). https://doi.org/10.16046/j.cnki.issn2096-5680.2020.03.006.
Ma, D.D., Ren, S.Y., Ma, T.Y., et al., 2023. Review on study of nanofluids heat transfer enhanced. Contemp. Chem. Res. (14), 7–9 (in Chinese). https://doi.org/10.20087/j.cnki.1672-8114.2023.14.003.
Naik, B., Soudagar, M.E.M., Thomas, M., et al., 2020. Numerical investigation of double pipe heat exchanger with different nanofluids conference. Series: Earth Environ. Sci. 573 (1), 012030. https://doi.org/10.1088/1755-1315/573/1/012030.
Patil, P.M., Shankar, H.F., 2022. Heat transfer attributes of Al_2O_3-Fe_3O_4/H_2O hybrid nanofluid flow over a yawed cylinder. Propul. Power Res. 11 (3), 416–429. https://doi.org/10.1016/j.jppr.2022.06.002.
Sahin, B., Manay, E., Akyurek, E.F., 2015. An experimental study on heat transfer and pressure drop of CuO-Water nanofluid. J. Nanomater. 2015 (1), 790839. https://doi.org/10.1155/2015/790839.
Sun, W., Cheng, Q.L., Wang, P.D., et al., 2016. Numerical simulation of steam coil heating process for large floating roof oil tank. Chem. Eng. 44 (7), 19–23. https://doi.org/10.3969/j.issn.1005-9954.2016.07.005 (in Chinese).
Sun, W., Cheng, Q.L., Zhao, L.X., et al., 2021. Energy loss analysis of the storage tank coil heating process in a dynamic thermal environment. Appl. Therm. Eng. 189, 116734. https://doi.org/10.1016/j.applthermaleng.2021.116734.
Sun, W., Liu, Y.D., Li, M.Y., et al., 2023. Study on heat flow transfer characteristics and main influencing factors of waxy crude oil tank during storage heating process under dynamic thermal conditions. Energy 269, 127001. https://doi.org/10.1016/j.energy.2023.127001.
Sun, C.J., Sun, B.M., Zhong, Y.F., et al., 2015. Numerical simulation of heat transfer enhancement by CuO-H_2O nanofluid. Therm. Energy Power Eng. 30 (2), 200–204 (in Chinese). https://doi.org/10.16146/j.cnki.rndlgc.2015.02.006.
Saleem, K.B., Marafie, A.H., Al-Farhany, K., et al., 2023. Natural convection heat transfer in a nanofluid filled l-shaped enclosure with time-periodic temperature boundary and magnetic field. Alex. Eng. J. 69, 177–191. https://doi.org/10.1016/j.aej.2022.12.030.
Wang, X.D., 2018. Optimization of the tubular heating process scheme for crude oil storage tanks. Pet. Petrochem. Energy Conserv. 8 (7), 27–29–10 (in Chinese). https://doi.org/10.3969/j.issn.2095-1493.2018.07.011.
Wang, B.B., Wang, G.X., Gao, Y., et al., 2022. Research on the mechanism of particle aggregation on the thermal conductivity of water-based copper nanofluids. J. Northeast. Electr. Power Univ. 42 (3), 83–90 (in Chinese). https://doi.org/10.19718/j.issn.1005-2992.2022-03-0083-08.
Wu, Y.D., 2022. Numerical simulation study on the heating process of spiral tubes in floating roof oil tanks. Pet. Petrochem. Energy Conserv. 12 (10), 19–23 (in Chinese). https://doi.org/10.3969/j.issn.2095-1493.2022.10.005.
Wei, Y.B., 2022. Research on Flow and Heat Transfer Characteristics of Nanofluid in Composite Enhanced Heat Transfer Technology. Zhengzhou University. Master's thesis (in Chinese). https://doi.org/10.27466/d.cnki.gzzdu.2022.000514.
Xie, X.F., Zhou, K., Zhou, L.Y., et al., 2021. Numerical simulation of temperature field in floating top oil tanks under solar radiation. Oil Gas Storage Transp. 40 (1), 107–112 (in Chinese). https://doi.org/10.6047/j.issn.1000-8241.2021.01.017.
Yu, L.L., 2014. Economic comparison of heat medium for tank-type heat exchangers. Petrochem. Equip. Technol. 35 (2), 62–65, 8 (in Chinese). https://doi.org/10.3969/j.issn.1006-8805.2014.02.020.
Yang, Z., Zhang, Z.R., Nie, H.C., 2020. Al_2O_3-H_2O numerical simulation of flow characteristics of nanofluids in tubes. J. Hunan Univ. Sci. Technol. (Nat. Sci. Ed.) 35 (2), 90–94 (in Chinese). 10.13582/j.cnki.1672-9102.2020.02.013.
Yang, L., Zhao, J., Dong, H., et al., 2018. Research on temperature profile in a large scaled floating roof oil tank. Case Stud. Therm. Eng. 12, 805–816. https://doi.org/10.1016/j.csite.2018.10.009.
Zhao, J., 2013. Heat-Transfer Research and Process Scheme Optimization of Oil Storage in Alpine Cold Region. Northeast Petroleum University. Doctoral dissertation (in Chinese).
Zhao, J., Dong, H., Wang, X.L., et al., 2017a. Research on heat transfer characteristic of crude oil during the tubular heating process in the floating roof tank. Case Stud. Therm. Eng. 10, 142–153. https://doi.org/10.1016/j.csite.2017.05.006.
Zhao, J., Dong, H., Fu, X.M., et al., 2017b. Cooling and gelatinization rule of waxy crude oil during static storage in floating roof tank. CIE J. 68 (12), 4882–4891 (in Chinese). https://doi.org/10.11949/j.issn.0438-1157.20170788.
Zhao, J., Liu, J.Y., Dong, H., et al., 2020. Numerical investigation on the flow and heat transfer characteristics of waxy crude oil during the tubular heating. Int. J. Heat Mass Tran. 161, 120239. https://doi.org/10.1016/j.ijheatmasstransfer.2020.120239.
Zhao, J., Lei, M.Y., Jiang, M.Z., et al., 2023a. Effect of mechanical stirring on the tubular heating process of crude oil. Int. J. Heat Mass Tran. 211, 124213. https://doi.org/10.1016/j.ijheatmasstransfer.2023.124213.
Zhao, J., Zhuo, Z.W., Dong, H., et al., 2023b. A new method for observation of microstructure of waxy crude oil and its emulsion system. Chem. Ind. Eng. Prog. 42 (8), 4372–4384 (in Chinese). https://doi.org/10.16085/j.issn.1000-6613.2022-1821.
Zhao, J., Li, F., Qu, C.L., et al., 2025a. Numerical simulation of tubular heating in waxy crude oil vault tank based on VOF model. Appl. Therm. Eng. 262, 125083. https://doi.org/10.1016/j.applthermaleng.2024.125083.
Zhao, J., Lei, M.Y., Liu, S.Q., et al., 2025b. Energy and heat transfer analysis on the heating process of crude oil tank with mechanical stirring. Pet. Sci. 22 (3), 1307–1339. https://doi.org/10.1016/j.petsci.2024.12.020.
Zhao, W.Q., 2021. Research on Heat Transfer Law of Tubular Heating Process of Crude Oil Storage Tank. Northeast Petroleum University. Master's thesis (in Chinese). https://doi.org/10.26995/d.cnki.gdqsc.2021.000507.
Zhao, P.J., 2024. Optimization of Electromagnetic Heating Pipeline Unblocking Structure and Energy Consumption Analysis. Xi'an Petroleum University. Master's thesis (in Chinese). https://doi.org/10.27400/d.cnki.gxasc.2024.000543.